

Chapter 1

Functional modelling of idiopathic pulmonary fibrosis

In Chapter 4, HRCT based quantitative analysis and shape analysis methods were developed to provide a consistent way of describing the features and progressions of IPF disease. However, it is not clear how - or whether - the spatial distribution of tissue abnormalities in IPF (including classifications of tissue type) correlate with lung function and their change over time. Translating these imaging and shape bio-markers into functional bio-markers to directly help with clinical diagnosis and treatment is still a challenge in progress. For the patient with IPF, V/Q mismatching and hypoxaemia are frequent occurrences. Computational modelling provides a novel way to understand how changes to the lung tissue contribute to observed decline in lung function, therefore modelling can potentially be used to build a relationship between image-based bio-markers and functional presentations. This chapter outlines an approach to functional modelling of IPF. The quantitative tissue-level and shape-level features described in previous chapters were combined with pulmonary function tests (PFTs) to guide a patient-specific

computational model of lung function in IPF. The lung function of healthy older adults was also modelled for comparison with the IPF models. This chapter therefore aims to integrate data from volumetric imaging, PFTs, and computational models of lung function, to understand differences between IPF and normal older lungs. Hypoxaemia in IPF has been suggested to be caused by either increased V/Q mismatch, anatomical shunts, or thickening of the gas exchange barrier. Swan (2010) showed that whole lung gas exchange is more sensitive to tissue stiffness (i.e. via V/Q mismatch) than gas exchange barrier thickness. Therefore, this chapter seeks to confirm whether stiffening-induced V/Q mismatch is sufficient to explain hypoxaemia in IPF. Lung function in IPF has been described in Chapter 2, and lung function in healthy older people will be introduced in Section 1.1. However, lung function is expected to decline with age even in normal individuals. Therefore, expected respiratory function in older people is first introduced, and then computational models aiming to reproduce this function are described.

1.1 Respiratory structure and function in older people

The respiratory system of the human keeps developing throughout life, with the peak-point of pulmonary function achieved before 30 years of age (Janssens et al., 1999; Sprung et al., 2006). For most people, respiratory performance begins to gradually decline after reaching this maximal status. The ability of the lung to deliver more oxygen to tissues than they require ("reserve capacity") decreases by about four-fold from age 20 to age 70 in healthy people (Smith, 1986; Zaugg and Lucchinetti, 2000). Even in older athletes who experience vigorous endurance exercise and have better aerobic ability, the functional capability of the lung will progressively deteriorate over time (Mittman et al., 1965; Pollock et al., 1997; McClaran et al., 1995).

Ageing-related changes in respiratory physiology are usually associated with structural alterations in both lungs, dilatation of alveoli, enlargement of airspaces, a decrease in gas exchange surface area, and increased residual volume (RV) and functional residual capacity (FRC) (Sprung et al., 2006; Lalley, 2013). There is a reduction in chest wall compliance and the static elastic recoil of the lung, which will lead to static air-trapping, a decrease in vital capacity (VC), a decrease in expiratory flows and an increasing work of breathing compared with younger individuals (Sprung et al., 2006). The strength of respiratory muscles decreases with age, and this is strongly correlated with nutritional status (lean body mass, body weight) and cardiac index (Janssens et al., 1999). The V/Q ratio heterogeneity tends to increase because of closing of dependent airways, and carbon monoxide transfer capability also decreases which is associated with the reduced alveolar surface area (Janssens et al., 1999). Interestingly, despite these changes, some research indicated that gas exchange may be preserved both at rest and during exertion, with only a slight reduction in arterial oxygen tension, and no significant change in arterial carbon dioxide tension, but pulmonary reserve is diminished (Janssens et al., 1999; Sprung et al., 2006). These age-associated changes are summarized in Table 1.1.

1.1.1 Ageing-associated alterations in the chest wall and respiratory muscle function

Several morphological changes occur in chest wall and diaphragm in older people that reduce the efficiency of the respiratory system. One of the most important changes is a progressive decline in chest wall compliance, which relates to a decrease in cross sectional area of the intercostal muscles, calcification of costal cartilage and rib-vertebral articulations, and narrowing of intervertebral disk spaces (Murray, 1986; Crapo, 1993).

Table 1.1: Age-associated changes in respiratory function and their relationships to clinical presentations (Reproduced from (Sprung et al., 2006; Lalley, 2013))

Measurements	Changes, ≥ 60 yrs.	Clinical presentations
Static lung volumes		
- TLC	Unchanged	
- FRC	Increase	
- IRV	Modest increase	
- ERV	Increase	
- V_T	Modest increase	
- VC	Decrease	
- IC	Increase	
- RV	Increase	Impaired gas exchange
Dynamic lung volumes		
- FVC	Decrease	
- FEV ₁	Decrease	
- FEV ₁ /FVC	Decrease	
- Peak expiratory flow	Decrease	
Resistance and compliance		
- Respiratory system resistance	Increase	
- Small airways closure	Increase	Impaired gas exchange
- Chest wall compliance	Decrease	Increase in work of breathing
- Lung compliance	Increase	Decrease in ventilatory response to exercise
Respiratory (muscle) pressures		
- Mean pleural pressure	Unchanged	
- Respiratory muscle strength	Increase	
Gas transfer		
- Ventilation-perfusion mismatch	Increase	Impaired gas exchange
Altered control of breathing		
- Responsiveness to imposed respiratory loads	Decrease	Hypoventilation
- Responsiveness to hypoxemia and hypercarbia	Decrease	Hypoxemia and hypercarbia
- Sensitivity to anesthetic agents and opioids	Increase	Respiratory failure in early postoperative period

TLC: total lung capacity; FRC: functional residual capacity; IRV: inspiratory reserve volume; ERV: expiratory reserve volume; V_T : tidal volume; VC: vital capacity; IC: inspiratory capacity; RV: Residual volume; FVC: forced vital capacity; FEV₁ : forced expiratory volume in 1 s; FEV₁/FVC : the ratio of the forced expiratory volume in the first one second to the forced vital capacity of the lungs.

The structural changes that occur in the chest wall are associated with a reduction in the curvature of the diaphragm and in the maximal transdiaphragmatic pressure, however the thickness of the diaphragm seems not to change significantly in older adults (Zaugg and Lucchinetti, 2000; Sprung et al., 2006). It is noted that age-associated osteoporosis results in a shape change of the thorax geometry; that is, an increase in dorsal kyphosis and anterior-posterior chest diameter (Janssens et al., 1999; Sprung et al., 2006).

The reduction in respiratory muscle strength that leads to age-related decrease of maximal static inspiratory and expiratory pressures will lead to lower efficiency of respiratory muscle activity (Wijesinghe and Dow, 2005; Sprung et al., 2006; Lalley, 2013). It has been shown that the reduced respiratory muscle strength is associated with a deficient nutritional status in older people, and a strong relationship has been found between maximal inspiratory/expiratory pressure and lean body mass (Arora and Rochester, 1982; Janssens et al., 1999). The electromyographic signal produced by twitch stimulation decreases by around 50% in 70-year-olds compared with young subjects, and this reduction is attributed to the loss of type II fast-twitch muscle fibres (Larsson, 1983).

1.1.2 Ageing-associated alterations in pulmonary mechanics and lung volumes

Although the chest wall becomes stiffer in older people, their lung parenchyma actually becomes more compliant (Mittman et al., 1965; Turner et al., 1968; Zaugg and Lucchinetti, 2000). The elastic recoil pressure of lung tissue gradually reduces with ageing, at a rate of around 0.1 to 0.2 cmH₂O on average every year (Turner et al., 1968), and this reduction is attributed to the alterations in the spatial distribution of the elastic

fibre network in the lung parenchyma (Sprung et al., 2006). In older people, the static pressure-volume curve of the lung is shifted to the left; in contrast, the pressure-volume curve of the thorax is shifted to the right (Zaugg and Lucchinetti, 2000; Sprung et al., 2006).

The tidal volume also experiences a slight decrease with age, whereas the respiratory rate gradually increases (Sprung et al., 2006). As mentioned in Section 1.1.1, the chest wall becomes stiffer with age, while the lung tissues become more compliant. These changes will lead to an increase in RV and a decrease in VC (Lalley, 2013). Some research has indicated that RV increases by approximately 50% from a 20-year-old to a 70-year-old on average, and VC will drop to around 75% of its peak value during this period, with a decrease of 20 to 30 ml per year (Janssens et al., 1999; Sprung et al., 2006). The TLC, which is the air volume in the lungs during a maximum inspiratory effort, remains unchanged with age, as the effect of the decreased inward elastic recoil of the lung is offset by the reduction in the outward elastic recoil of the chest wall (Sprung et al., 2006). However, FRC increases by 1 to 3% per decade, since the rate of decrease in lung recoil exceeds the rate of decrease in chest wall compliance (Janssens et al., 1999; Lalley, 2013). Forced vital capacity (FVC) and forced expiratory volume in one second (FEV_1) have been demonstrated to decrease progressively with ageing in both men and women (Knudson et al., 1976), but these measurements decrease more rapidly in males than in females (Crapo, 1993). FEV_1 decreases by approximately 20 ml per year in subjects aged 25 to 29 years, but for people more than 65 years old, the average annual rate of reduction is more dramatic: up to 38 ml (Brandstetter and Kazemi, 1983).

1.1.3 Ageing-associated alterations in gas exchange

The inhomogeneity or "mismatch" in ventilation and perfusion increases with age, especially in the gravitationally dependent regions of the lung where intrapleural pressure becomes higher with age, and as the lung tissues become less elastic, they fail to keep small airways open (Holland et al., 1968; Paoletti et al., 1985; Lalley, 2013). The increased ventilation-perfusion heterogeneity results in a reduction in P_aO_2 , with a progressive drop from approximate 95 mmHg at 20 years to about 75 mmHg at 70 years. However, $PaCO_2$ remains almost unchanged with increasing age, although PaO_2 declines (Wahba, 1983; Sprung et al., 2006). This can possibly be explained by a decreased rate of basal metabolism and a higher diffusive capability of CO_2 across the alveolar-capillary membrane (Levitzky, 1984). Local pulmonary perfusion can also reduce with age in some regions that are well ventilated as a result of reduced cardiac output (Levitzky, 1984; Lalley, 2013). The alveolar-arterial pressure difference for oxygen ($P_{A-a}O_2$) increases with ageing due to the increased heterogeneity of V/Q, and this change is probably also related to the increase in closing volume during breathing (Janssens et al., 1999). It can be observed that PaO_2 reduces at a rate of approximately 5 mmHg per decade from the age of 20 years. Additionally, the diffusing capacity of the lungs for carbon monoxide (DLCO) decreases with age (Guenard and Marthan, 1996), with loss of about $0.3 \text{ mL}\cdot\text{min}^{-1}\text{mmHg}^{-1}$ and $0.2 \text{ mL}\cdot\text{min}^{-1}\text{mmHg}^{-1}$ per year for men and women, respectively (Murray, 1986). The reduction is more significant after 40 yrs of age, and the increased mismatch in V/Q, a decline in the alveolar surface area (Verbeken et al., 1992; Thurlbeck and Angus, 1975), the decreased density of lung capillaries (Butler and Kleinerman, 1970) and the reduction in pulmonary capillary blood volume (Guenard and Marthan, 1996) are all potential factors that may cause a reduced

diffusion capacity.

1.1.4 Relationship between lung function and lung shape

There is strong evidence that age-related changes in lung structures are associated with a series of alterations in respiratory function (introduced in Section 1.1). For example, the reduction in chest wall compliance of older people leads to a decrease in VC, while an increased RV in the elderly usually results in impaired capability of gas exchange which relates to a lower measured DLCO. In a previous study (Osanlouy, 2018), several lung structure-function relationships were analysed through quantifying the correlations between the first three PCA-based mode weights calculated for a SSM of a healthy cohort aged 20-90 years with age, BMI, lung volume and some pulmonary function measurements. For each training subject of this SSM, the individual weight scores for each of the first three shape modes (which captures most shape variation) were examined. An ordinary least squares regression was applied to test the associations, and the P-value was used to quantify the strength of each association, with an alpha level of 0.05 considered statistically significant. Analysis showed that Mode 1 is positively correlated with FEV₁, FEV₁/FVC, Maximal mid-expiratory Flow (FEF25%-75%), BMI and DLCO, whereas it is negatively correlated with age, RV and RV/TLC. For Mode 2, only BMI is found to be correlated with the shape variation, whereas quite a number of lung volume measurements (including FRC, TLC ,VC and RV) showed strong relationships with Mode 3.

1.2 Methods: Patient-specific modelling of IPF lung function

In this section, a patient-specific computational model of lung function is proposed to explore V/Q matching and whole lung gas exchange for patients with IPF. In order to make a comparison of lung function between the IPF patient and older normal people, for each patient, a subject-specific lung mesh that represents the statistical lung shape of a normal individual of the same age, BMI and pulmonary function data was predicted using an SSM. Anatomically-based airway and blood vessel trees were generated from HRCT images of IPF subjects, and for the corresponding normal lung mesh. Ventilation, perfusion, and gas exchange were simulated in the IPF and control models under baseline healthy conditions, and with constriction of airways and/or blood vessels in tissue regions classified as abnormal. To achieve this, the individual's lung parenchymal tissue classification and quantification data was mapped to their spatial model, with fibrosis assumed to reduce tissue compliance and narrow vessels. Data from PFTs were used to parameterize the models and set the boundary conditions for simulation. The modelling framework is illustrated in Figure 1.1.

1.2.1 Clinical data

Two patients diagnosed with IPF were selected from the clinical data used in Chapter 4 as representative subjects for functional modelling. Patient 1 is female with three imaging time points at 0, 12 and 23 months, and Patient 2 is a male with two time points at 0 and 46 months. The clinical data for each patient includes both HRCT images and PFT results, with less than 3 months between the scan date and the PFT date.

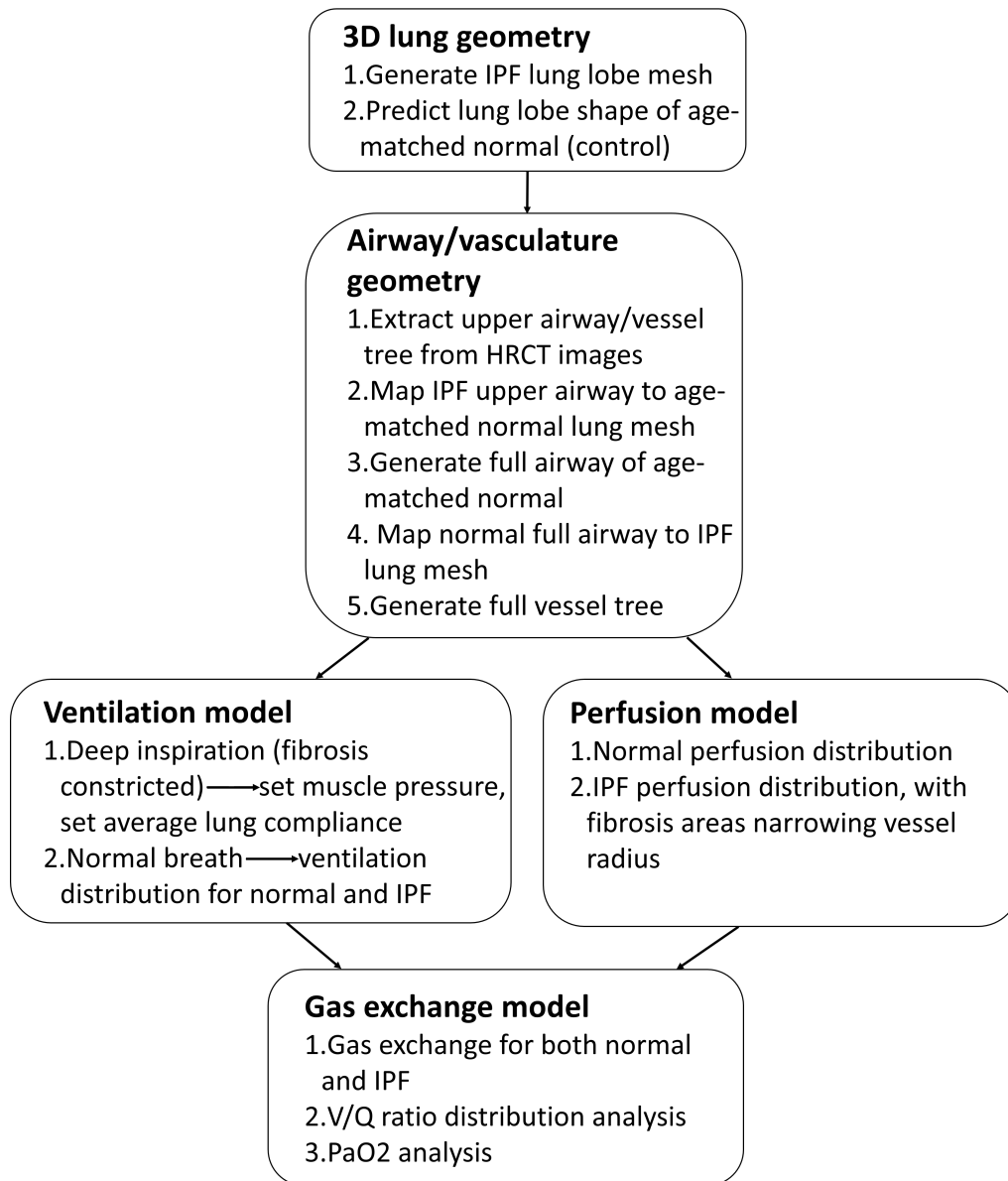


Figure 1.1: Computational modeling framework for IPF and older normal lung function.

1.2.2 Construction of lung lobe geometry

In Chapter 4, Section ?? and ??, the lung lobe shapes and volumes of an IPF cohort were compared with a normal older (control) cohort with a similar age range. It was shown that there is a significant difference in lung lobar geometry between IPF and older controls. This alteration in lung shape is mainly basal (lower lobe), and is strongly associated with the distribution of fibrosis in IPF. In order to include the impact of shape change into the modelling of lung function, the SSM of a normal older cohort and the IPF patient's individual information were combined to predict a lung lobe shape of an age-matched normal as a control model to compare to each IPF patient. The lung lobe mesh of each IPF patient was generated using the method introduced in Chapter 3, Section ??.

The SSM used to predict the age-matched control model in this chapter is different from Osanlouy (2018), because it only includes subjects aged 50 years and over. Underlying relationships with lung function are still expected to be present, however.

Shape prediction of a normal lung to correspond to each IPF patient

A lung shape prediction model for a healthy cohort aged ≥ 50 years was developed based on a previous analysis of lung structure-function relationships (Osanlouy, 2018). Age, BMI, FVC, FEV₁, FRC, TLC, VC, RV, RV/TLC and DLCO were selected as the individual functional measurements to train the lung shape predictive model, as these parameters have been shown to have relatively strong correlations with the first three shape modes. The training process for the lung shape predictive model was to find optimized equations that best describe the relationship between the functional measures and the mode weights. For each shape mode, a multivariate regression model was con-

structed as:

$$w_i = \alpha_{0i} + \alpha_{1i}m_1 + \alpha_{2i}m_2 + \dots + \alpha_{ni}m_i + \varepsilon, \quad (1.1)$$

where w_i is the weight score of the i th shape mode, n is the number of functional measures, $\alpha_{0i}, \alpha_{1i}\dots\alpha_{ni}$ are the regression coefficients (in which α_{0i} is the intercept) m_i is the tested value of the i th functional measure, and ε is a random error.

Using Equation 1.1, a set of possible regression models can be developed for each shape mode (with different regression coefficients $\alpha_{0i}, \alpha_{1i}\dots\alpha_{ni}$). In order to find the best predictive model from all possible models, the two most common criterion for model selection - the Akaike information criterion (AIC) and the Bayesian information criterion (BIC) - were used to deal with the trade-off between the goodness of fit of the model and the simplicity of the model (Aho et al., 2014). Both AIC and BIC are founded on information theory, with each calculated by

$$AIC = 2k - 2\ln L(\theta), \quad (1.2)$$

$$BIC = \ln(n)k - 2\ln L(\theta), \quad (1.3)$$

where k is the number of the estimated parameters (that is the number of functional measures in this study) in the model, $L(\theta)$ is the maximized value of the likelihood function of the model and θ are the parameter values that maximize the likelihood function.

The multivariate regression models with the lowest values of AIC and BIC were selected as the best predictive models, then the models of the first three PCA modes were constructed in the form of Equation 1.1, as

$$\begin{aligned}
 w_1 &= 1.38 + (-0.04 \times \text{Age}) + (0.38 \times \text{FVC}) + (-0.04 \times \text{DLCO}), \\
 w_2 &= 3.49 + (-0.16 \times \text{BMI}) + 0.02 \times \text{RV/TLC}, \\
 w_3 &= 4.90 + (-0.02 \times \text{Age}) + (-0.45 \times \text{TLG}) + (-0.05 \times \text{DLCO}),
 \end{aligned} \tag{1.4}$$

where w_1 , w_2 and w_3 are the weight scores of the first three shape modes. By inputting the individual functional measures into the regression models, the weights of the first three modes are calculated. Then the subject-specific predicted shape of the control lung model is reconstructed by adding the linear combination of the first three modes to the average SSM

$$S_{pred} = S_{mean} + \sum_{i=1}^3 \mathbf{u}_i w_i, \tag{1.5}$$

where S_{mean} is the mean of the SSM for the older normal cohort, and S_{pred} is the subject-specific predicted lung shape.

1.2.3 Construction of airway/vascular geometry

Subject-specific conducting airway trees and pulmonary vasculature trees were constructed for both the actual shape of the IPF patient's lung and control model with the same characteristics of that subject. The geometry of the pulmonary airway and vessels are important subject-specific features. In this study, airway/vessel trees were first generated for the predicted control model, which represents a healthy lung matched to the IPF subjects. The models were then deformed to the shape of the IPF lung mesh which has quantifiable shape differences as described in Chapter 4. The airway/vasculature diameters were assigned to each branch as a postprocessing step, with values appro-

priate for a healthy lung and for IPF. In this way, the branches for the IPF and control airway/vascular models retain the same geometric connectivity and same lobar distribution, but have different radius and length.

Airway tree

In order to generate an airway tree in the lung shape, the bi-cubic Hermite finite element mesh of the lung surface was converted to a tri-cubic Hermite volumetric mesh (introduced in Chapter 4, Section ??). An anatomically-based structure of the bronchial airways (from trachea to terminal bronchioles) was generated using the methods described in detail by Tawhai et al. (2004). In brief, the centrelines of the largest airways (trachea, and left and right branches of the first 6 generations of airways) were manually segmented from the subject's HRCT images. This provides an incomplete description of the airway tree. Then, the larger airways were used as an initial condition to generate the remaining branches down to the level of the terminal bronchioles within the subject's lung mesh using a volume-filling branching algorithm. The steps to generate patient-specific airways in IPF and old normal lungs are summarized as follows:

1. 1-D finite element mesh of the centerlines of IPF larger airways were created manually from HRCT raw images of the IPF patient (shown in Figure 1.2a).
2. The 1-D tree of central airways was mapped to the volumetric mesh of the control model. The nodal positions inside the control mesh were mapped by calculating the local coordinate ξ_i with respect to its element (details in Chapter 4, Section ??). The branches outside the mesh were then scaled to match the target lung volume, followed by a manual adjustment. The element connectivity remained the same during mapping.
3. The mapped larger airways in step 2 was used as a starting geometry for generating a full airway tree by using a volume-filling branching algorithm (Tawhai et al.,

2004), to fill the shape of the control mesh. Briefly, a uniformly-spaced grid of seed points was created within the 3D volumetric lung mesh. The number of seed points was ~ 32000 (45% for left lung and 55% for right lung) which approximates the number of pulmonary acini in the lung (Haefeli-Bleuer and Weibel, 1988). The branching algorithm was designed to generate a branching structure recursively towards the center of mass of seed point groupings, until each seed point was assigned to a terminal bronchiole (shown in Figure 1.2b).

4. The generated linear mesh of the full airway tree in step 3 was mapped back to the volumetric lung mesh of the IPF patient using the same method as in step 2.

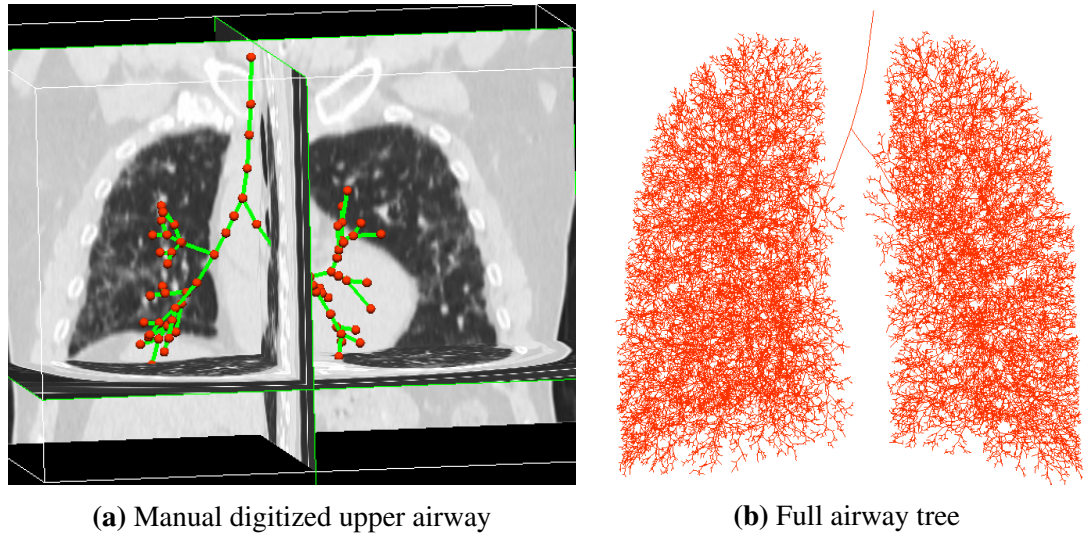


Figure 1.2: Generation of airway tree. (a) Manual digitized upper airway tree from HRCT images in 3D. Blue lines are the centerlines of upper airway tree, and red points represent airway nodes. (b) Geometry of full conducting airway tree generated using volume-filling algorithm. The model is shown from the anterior view, with the left lung on right, and right lung on left.

In the next stage, the diameters of the airway branches were assigned for both IPF and control models. The method was:

1. The trachea radius for IPF was measured from segmented HRCT images (based

on the segmented cross-section of larger airway branches) at 25%, 50%, and 75% along the centreline of the trachea. The trachea radius was defined as the average of the three measurements.

2. The radius of the terminal bronchioles in the control models were assumed to be 0.2mm (Horsfield et al., 1976). The airways in the IPF lung have been found to be narrowed in 70% of patients (Crystal et al., 1976). The terminal bronchiole radius for the IPF models was therefore scaled to a smaller value. The scaling was assumed to be in proportion to the ratio of IPF to control model volumes, as:

$$R_{TB_{IPF}} = R_{TB_{Control}} \times \sqrt[3]{\frac{FRC_{IPF}}{FRC_{Control}}}, \quad (1.6)$$

where FRC_{IPF} is the measured FRC volume for the IPF patient and $FRC_{Control}$ is the reference FRC volume for the control model, $R_{TB_{IPF}}$ is the terminal bronchiole radius in the IPF models, and $R_{TB_{Control}} = 0.2\text{mm}$ is the terminal bronchiole radius in the reference (i.e. control) model.

3. The radii of the other airway branches for the IPF models were calculated by assuming a constant Horsfield diameter ratio (R_dH) for each IPF subject. R_dH is the rate of reduction of diameter (or radius) with reduction in Horsfield order, with R_dH calculated by:

$$R_dH = \frac{10 \times (\log_{10} R_{TB} - \log_{10} R_{Trachea})}{1 - H_{Trachea}}, \quad (1.7)$$

where R_{TB} is the terminal radius, $R_{Trachea}$ is the trachea radius, and $H_{Trachea}$ is the Horsfield order of the trachea.

4. While the R_{TB} is expected to be smaller in IPF (Crystal et al., 1976), the anatomical deadspace (V_D) is actually larger (Plantier et al., 2016). $R_{Trachea}$ and R_dH for the

control models were therefore set such that V_D (control) < V_D (IPF), for $R_{Trachea}$ within the normal published range for men (6.5-12mm) and women (5-11mm) (Breatnach et al., 1984). V_D (control) was initialized using V_D (control) = V_D (IPF) \times (34.2/45.3), which is a relationship measured by Plantier et al. (2016) for IPF and controls. $R_{Trachea}$ and R_dH were adjusted until $R_{Trachea}$ was within the normal size range.

Using the above steps, a patient-specific pulmonary airway geometry for IPF and the control lung was constructed.

Vascular tree

The centerlines of the first two generations of vessel trees were manually segmented from HRCT images, and represented as a 1-D finite element mesh. In this thesis, the pulmonary arterial and venous trees of other generations were assumed to be approximate replicas of the airway tree. Using the airway tree to approximate vessel geometry is a reasonable assumption, as the conventional pulmonary arteries generally follow the same branching pattern as the airways trees, and the airways and blood vessels have similar lengths and orientations. The airway and vasculature have been observed to bifurcate in union from larger branches to the bronchiole level, and the veins to divide at the approximate midpoint between adjacent airway bifurcations (Weibel, 1984; Hsia et al., 2016). The manually-segmented main vessels plus the finite element model of the airway tree provided a full pulmonary blood vessel geometry for the IPF patient. The vascular structure for the control model was obtained using the same mapping procedure used for the airways as described previously. The microcirculatory model of Clark et al. (2010, 2011) was appended to each terminal arteriole, to supply a corresponding terminal venule. This model is a symmetric-branching system of arterioles and venules that are connected (from arteriole to venule) at each generation by a recruitable and

distensible "capillary sheet".

The unstrained (zero transmural pressure (P_{tm})) radius of the main pulmonary artery ($R_{mArtery}$) and vein (R_{mVein}) were assigned based on the patient-specific (measured) trachea radius and data from morphometric studies (Equation 1.8and 1.10) (Horsfield, 1978; Horsfield and Gordon, 1981; Huang et al., 1996). The radius of all other arteries and veins down to the distal level were calculated based on a defined rate of increase in diameter with vessel Strahler order, the Strahler diameter ratio for artery and vein (R_dS_{Artery} and R_dS_{Vein}). The value of R_dS for the arterial tree and venous tree were specified according to the radius of the main artery and vein, and aiming for consistency with published human data (Horsfield et al., 1971; Horsfield, 1978; Horsfield and Gordon, 1981; Huang et al., 1996):

$$R_{mArtery} = \frac{k_{Artery} \times R_{Trachea}}{R_{Trachea_{ref}}}, \quad (1.8)$$

$$R_dS_{Artery} = \frac{10 \times (\log_{10} R_{sArtery} - \log_{10} R_{mArtery})}{1 - S_{mArtery}}, \quad (1.9)$$

$$R_{mVein} = 10 \times \log_{10} \left(\frac{k_{Vein} \times R_{Trachea}}{\log_{10} R_{Trachea_{ref}}} \right), \quad (1.10)$$

$$R_dS_{Vein} = \frac{10 \times (\log_{10} R_{sVein} - \log_{10} (k_{Vein} \times R_{Trachea}))}{3 - S_{mArtery}}, \quad (1.11)$$

where k_{Artery} is constant artery radius (equals to 11.53), k_{Vein} is a constant for vein radius (equals to 6.3), $R_{Trachea_{ref}}$ is a statistical reference trachea radius (equals to 9 mm), $R_{sArtery}$ is the target for smallest arteries (equals to 0.125 mm), R_{sVein} is the target for smallest veins (equals to 0.125 mm), and $S_{mArtery}$ is the Strahler order of the

artery model. The vessel radius for the IPF models and the control models were then calculated.

1.2.4 Construction of computational models

In this chapter, computational modelling of lung function integrates previously published models of ventilation (Swan et al., 2012), perfusion (Clark et al., 2010, 2011) and gas exchange (Clark et al., 2014) to simulate \dot{V}/\dot{Q} distribution and oxygen and carbon dioxide exchange during tidal breathing in the upright posture. The patient-specific geometry of airways and vessels were used as input for these models. A brief introduction of the model components is summarized below, and details can be found in the referenced papers.

Ventilation model

The ventilation model developed by Swan et al. (2012) was used to predict the time-averaged topological distribution of inhaled air in the upright human lung, governed by local tissue deformation, elastic recoil pressure, airway resistance and acinar compliance. Each of the acini in the tree model subtending each terminal bronchiole are assumed to function as compliant compartments. The acinar volume and compliance were initialised at FRC using a distribution of tissue strain along the gravitational direction that was consistent with strain computed by a tissue mechanics model (Tawhai et al., 2009). The acinus volumes were perturbed around these values to provide variability as observed in the lung (a coefficient of variation of 0.1). Compliance of each acinus was calculated using a relationship between volume and compliance for isotropically expanding units of tissue in the Tawhai et al. (2009) tissue mechanics model.

Compliance C, is defined by

$$C = \left[\frac{\xi e^\gamma}{6V_0} \left(\frac{3(3a+b)^2(\lambda^2 - 1)^2}{\lambda^2} + \frac{(3a+b)(\lambda^2 + 1)}{\lambda^4} \right) \right]^{-1}, \quad (1.12)$$

where λ is the (isotropic) stretch, V_0 is the undeformed volume, and $\gamma = \frac{3}{4}(3a+b)(\lambda^2 - 1)^2$. The movement of air into each acinar unit was determined by expansion of the alveolar tissue and airway resistance.

In this model, the flow through the conducting airways was assumed to be Poiseuille with a "correction factor" to account for additional energy losses that occur in branching airways (Pedley et al., 1970). Additional energy losses caused by flow disturbances are created at the airway bifurcations and contribute to the calculation of pressure drop across the junction. A correction term, Z_{Pe} , was used to define the ratio of actual energy dissipation to Poiseuille flow dissipation, then the ratio of actual airway resistance (R_{aw}) to its Poiseuille flow equivalent (R_P) can be calculated by (ignoring kinetic energy changes):

$$Z_{Pe} = \frac{R_{aw}}{R_P} = \frac{K_{Pe}}{4\sqrt{2}} \left(R_e \times \frac{2r}{l} \right)^{0.5}, \quad (1.13)$$

where R_e is the Reynolds number, r and l are the radius and length of the airway, respectively. $R_e = \frac{2Q\rho}{\pi r \mu}$, where ρ and μ are the density ($1.51 \times 10^{-6} g.mm^{-3}$) and viscosity ($1.92 \times 10^{-5} P_a.s$) of air, respectively. K_{Pe} is a constant, set to 1.85. Then, the resistance of each airway branch was calculated as the Poiseuille resistance (R_{aw}) multiplied by the term Z_{Pe} , and the Poiseuille flow through each conducting airway was acquired by the following equation:

$$P_{aw_2} - P_{aw_1} = R_{aw} \dot{V} = Z_{Pe} R_P \dot{V} = Z_{Pe} \frac{8l\mu}{\pi r^4} \dot{V}, \quad (1.14)$$

where P_{aw_1} , P_{aw_2} are the air pressures at the start and end of a branch, and \dot{V} is the air flow through the airway. The air flow into the acinus (modelled as a compliant unit subtending the terminal bronchiole) was determined by an equation of motion that relates airway resistance, air flow, tissue compliance and the rate of change of internal and external pressures:

$$P_{aw} = \frac{V_A}{C_A} + R_{aw}\dot{V} + I\frac{d\dot{V}}{dt} - P_l, \quad (1.15)$$

where P_{aw} , R_{aw} and \dot{V} are the pressure, Poiseuille resistance and flow in the terminal bronchiole, V_A and C_A are the volume and compliance of the acinar unit, I is inertance of the unit, and P_l is an external driving pressure (varied sinusoidally) working to expand the unit and drive air flow through the conducting airways to the terminal units.

Here, we assumed that the rate of change of airflow \dot{V} is small enough, that the term $I\frac{d\dot{V}}{dt}$ in Equation 1.15 can be neglected. A suitable small time interval, $\Delta t = t_n - t_{n-1}$, was defined, and the flow at the end of the time period $\dot{V}_n = \dot{V}(t_n)$ is:

$$\dot{V}_n = C_A(\nu - \beta) + \dot{V}_{n-1} - C_A(\nu - \beta)\exp\left(\frac{-\Delta t}{R_{aw}C_A}\right), \quad (1.16)$$

where $\dot{V}_{n-1} = \dot{V}(t_{n-1})$ is the flow at the end of the previous time period. $\nu = dP_{aw}/dt$, and $\beta = dP_l/dt$ are the change of bronchiole pressure and driving pressure with respect to t , respectively. This equation is derived from Equation 1.15. The detailed description can be found in Swan et al. (2012).

Perfusion model

The pulmonary perfusion model developed by Clark et al. (2011) was used to simulate a time-averaged distribution of blood flow, capillary blood volume and average red blood

cell (RBC) transit time for each acinus unit. The full vascular structure (including arteries, veins, intra-acinar arterioles and venules, and capillaries) generated in Section 1.2.3 was the geometric domain for this model. Distension of blood vessels and hydrostatic effects were also included in the model, with arterial and venous diameter and the thickness of the capillary sheet assumed proportional to the transmural pressure (P_{tm}). The intra-acinar (extra-capillary) blood flow was modeled in the symmetric ladder structure introduced previously. The microcirculatory model relates the vessel diameter, length and the thickness of capillary sheet.

Similarly to air flow, the flow through pulmonary arteries and veins was predicted using a Poiseuille equation, with an additional term for gravitational effects acting on blood in the vessels. The relationship is given by

$$\Delta P = P_{b2} - P_{b1} = \frac{128\mu_b L \dot{Q}}{\pi D^4} + \rho_b L g \cos\theta, \quad (1.17)$$

where P_{b1} and P_{b2} are the blood pressures at the beginning and end of the vessel element, μ_b and ρ_b are the viscosity and density of the blood in the vessel, L and D are the vessel length and radius, \dot{Q} is the volumetric flow rate in the vessel, g is the gravitational acceleration ($9.81 m/s^2$), and θ is the angle between the vessel and the direction of gravity.

The term $\rho_b L g \cos\theta$ in Equation 1.17 represents the effect of gravity on blood in the vessels. In the microcirculatory model, an arteriole and venule were joined at each generation by a capillary bed, forming a "ladder-like" structure, to construct the intra-acinar circulation. Therefore, the term $\rho_b L g \cos\theta$ was considered negligible because the length of acinar arterioles and venules was assumed to be small enough, and

$$\Delta P = \frac{128\mu_b L \dot{Q}}{\pi D^4}. \quad (1.18)$$

The strained diameter D in Equation 1.18 was assumed to have a linear relationship with the transmural pressure P_{tm} as

$$\frac{D}{D_0} = \alpha P_{tm} + 1, \quad (1.19)$$

where D_0 is the unstrained vessel diameter, α is the vessel compliance constant. The tethering pressure acting on the blood vessel in the radial direction was assumed to be equal and opposite to the local tissue elastic recoil pressure (P_e), therefore $P_{tm} \approx P_b - P_e$, where P_b is the average blood pressure along the vessel. Then, the blood flow through a capillary sheet (\dot{Q}) was modelled using the classic sheet flow theory developed by Fung and Sabin (1969) as

$$\dot{Q} = \frac{SA}{\mu_c f l_C^2} \int H^3 dP_{tm}, \quad (1.20)$$

where A is the alveolar surface area, S is the proportion of alveolar surface area (A) composed of capillaries, μ_c is the apparent viscosity of blood in the capillaries, f is the numerical friction factor, l_C is the average path length through the capillary network between arteriole and venule. H is the thickness of the capillary sheet which was assumed to be approximately linearly dependent on P_{tm} similar to Equation 1.19

$$\frac{H}{H_0} = \alpha_C P_{tm} + 1, \quad (1.21)$$

where H_0 is the unstrained sheet thickness. In both Equation 1.19 and Equation 1.21, maximum P_{tm} was assumed to be $32\text{cmH}_2\text{O}(3.1\text{KP}_a)$. α_C is the compliance of the

capillary sheet, which was assumed to reduce linearly with increase of transpulmonary pressure (P_{tp})

$$\alpha_C(P_{tp}) = a + bP_{tp}, \quad (1.22)$$

where a and b are constants, P_{tp} is assumed to be equal and opposite to P_e . The values of a and b were firstly measured for dogs by Glazier et al. (1969), then scaled for human as $a = 0.165\mu m/cmH_2O$, $b = -2.58\mu m/(cmH_2O)^2$.

Gas exchange model

The ventilation and perfusion distribution predicted by the ventilation and perfusion models described in the previous section were used as inputs in a whole lung model of gas transport and exchange. The ventilation model provided the volume change in each acinus during inspiration and expiration. The perfusion model determined the acinar capillary blood volume and average RBC transit time. The modelling was based on the assumption that the acinus was well-mixed, and the ventilation and perfusion distributions were time-invariant. Then the rate of O_2 removal from the alveolar air and the rate of CO_2 transferred to the well-mixed alveolar compartment of the acinus were determined. The steady-state gas transfer model developed by Kapitan and Happleman (1986) and used by Clark et al. (2014) was used to predict the partial pressure of oxygen in alveolar air (P_AO_2) and in arterial blood (P_aO_2).

In each gas exchange acinar unit, the steady-state blood and gas compositions are related by conservation of mass. The equilibrium oxygen partial pressure was described through the relationship

$$\dot{V}_I P_{I_{O_2}} - \dot{V}_E P_{A_{O_2}} = k \dot{Q}_C (C_{C_{O_2}} - C_{\bar{V}_{O_2}}), \quad (1.23)$$

where \dot{V}_I is the unit's inspired ventilation (L/min), $P_{I_{O_2}}$ is the oxygen partial pressure (mmHg) of the humidified inspired air, \dot{V}_E is the expired (alveolar) ventilation (L/min), $P_{A_{O_2}}$ is the oxygen partial pressure (mmHg) of the alveolar air, k is a constant that accounts for differences in temperature and pressure between body and the atmosphere as well as allowing consistency between the units of the left and right hand side of Equation 1.23, \dot{Q}_C is the capillary blood flow, $C_{C_{O_2}}$ is the oxygen content in the end-capillary blood (ml gas/100 ml blood), and $C_{\bar{V}_{O_2}}$ is oxygen content entering the lungs from mixed venous blood (ml gas/100 ml blood). The O_2 and CO_2 contents are associated with the corresponding partial pressure of O_2 and CO_2 by the appropriate dissociation curve. The left-hand side of Equation 1.23 represents the volume rate of gas uptake from the compartment by the air, and the right-hand side represents the volume rate of gas uptake from the compartment by the blood. The rates are equal at steady-state.

The non-linear Monod-Wyman-Changeaux model (Monod et al., 1965) is used to solve the relationship between oxygen content and partial pressure. The oxygen content in the end-capillary blood $C_{C_{O_2}}$ in each acinus unit is related to the end-capillary oxygen partial pressure ($P_c O_2$) as

$$C_{C_{O_2}} = \frac{15 \times 1.34 \times \rho(P_c O_2) + 0.03 \times P_c O_2}{100}, \quad (1.24)$$

where $\rho(P_c O_2)$ is the oxygen saturation, and it is a function of $P_c O_2$. The oxygen binding capacity with haemoglobin is 1.34 mL oxygen per gram of hemoglobin, and around 15 g of hemoglobin per 100 mL of blood. Therefore, the term $15 \times 1.34 \times \rho(P_c O_2)$ expresses oxygen bound to haemoglobin. The term $0.03 \times P_c O_2$ expresses the

oxygen dissolved in blood plasma, which gives 0.03 mL of oxygen per 100 mL of whole blood for each mmHg of partial pressure.

The oxygen saturation $\rho(P_cO_2)$ was calculated from Monod-Wyman-Changeaux model (Monod et al., 1965) as

$$\rho(P_cO_2) = \frac{LK_T\sigma P_cO_2(1 + K_T\sigma P_cO_2)^3 + K_R\sigma P_cO_2(1 + K_R\sigma P_cO_2)^3}{L(1 + K_T\sigma P_cO_2)^4 + (1 + K_R\sigma P_cO_2)^4}, \quad (1.25)$$

where K_R (equals to $3.6 \times 10^6 L/mol^{-1}$) and K_T (equals to $10 \times 10^3 L/mol^{-1}$) are the microscopic dissociation constants of a single ligand bound to a stereospecific site, in the two states (R and T), respectively. L (equals to 171.2×10^6) is the equilibrium constant for the state R to T transition, and σ (equals to $1.4 \times 10^{-6} mol \cdot L^{-1} mmHg^{-1}$) is the oxygen solubility.

In this model, it is assumed that the blood stays in the capillaries long enough to achieve equilibrium between the alveolar air and capillary blood, and P_AO_2 can equilibrate with P_cO_2 at the end of each inspiration. Therefore, P_AO_2 and P_cO_2 can be solved from Equation 1.23 using Newton's method. The ventilation-weighted sum of P_AO_2 was calculated as an estimate of expired oxygen partial pressures from the full lung, and the perfusion-weighted sum of C_cO_2 was used to estimate the P_aO_2 .

The predicted acinus ventilation and perfusion were used as input into the gas exchange model, and carbon dioxide transport was also simulated using the same assumption of equilibration between air and blood similar to the oxygen transfer model (Kapitan and Happleman, 1986). In each acinus unit, equilibration of carbon dioxide between air side and blood side was represented through a mass balance equation

$$\dot{V}_A P_A CO_2 = k \dot{Q}_C (C_{CO_2} - C_{\bar{V}_{CO_2}}), \quad (1.26)$$

where \dot{V}_A is the expired or alveolar ventilation, C_{CO_2} is the carbon oxygen content in the end-capillary blood, and $C_{\bar{V}_{CO_2}}$ is carbon oxygen content entering the lungs from mixed venous blood. As in the calculation for oxygen exchange, the assumption that transport time is sufficient to equilibrate between blood and air for carbon dioxide exchange was used, so that $P_A CO_2$ can be predicted by solving Equation 1.26. $P_c CO_2$ in each acinus unit was calculated from C_{CO_2} using Henry's law

$$C_{CO_2} = \frac{M \cdot P_c CO_2}{1 + M \cdot P_c CO_2} (P_c CO_2 - P_v CO_2), \quad (1.27)$$

where M (equals to $23.86 ml \cdot mmHg^{-1}$) is the transfer factor for carbon oxygen across the capillary-alveolar membrane (Chakraborty et al., 2004), and $P_v CO_2$ is the partial pressure of oxygen in mixed venous blood.

Some parameter values used in the ventilation, perfusion and gas exchange models are listed in Table 1.2. More details of the models are given in Swan and Tawhai (2010), Swan (2010), Clark et al. (2011), and Swan et al. (2012).

1.2.5 Modelling lung function

Ventilation, perfusion and gas exchange models were solved under normal conditions (using lung and airway geometry for older normal people) and diseased conditions (using lung and airway geometry of IPF patients). Individual subject tissue classification from CALIPER was projected to the IPF airway/vessel trees as labelled disease regions to drive the patient-specific functional modelling of IPF, with fibrosis reducing tissue

Table 1.2: Parameter values and their source used in computational models

Parameter	Description	Value	Source
K_{Pe}	Pedley correction factor	1.85	Pedley et al. (1970)
p	Air density	$1.15 \times 10^{-6} g.mm^3$	Ideal gas law (37C)
μ	Air viscosity	1.92×10^{-6}	Sutherland's formula (37C)
α	Vessel compliance	$1.49 \times 10^{-4} Pa^{-1}$	Krenz and Dawson (2003)
μ_b	Blood viscosity	$3.36 \times 10^{-3} Pa/s$	Pries et al. (1996)
p_b	Blood density	$1.05 \times 10^{-6} kg/mm^3$	Pries et al. (1996)
μ_c	Apparent viscosity of blood in capillary bed	$1.92 \times 10^{-3} Pa/s$	Fung (2013)
f	Numerical friction factor	21.6	Fung (2013)
α_c	Compliance of capillary sheet	$1.30 \times 10^{-9} Pa/s$	Fung and Sabin (1969)
l_c	Pathlength from arteriole to venue	$11.86 \times 10^{-6} m$	Clark et al. (2010)
K_R	microscopic dissociation constant	$3.6 \times 10^6 L/mol^{-1}$	Monod et al. (1965)
K_T	microscopic dissociation constant	$10 \times 10^3 L/mol^{-1}$	Monod et al. (1965)
L	equilibrium constant	171.2×10^6	Monod et al. (1965)
σ	oxygen solubility	$1.4 \times 10^{-6} mol \cdot L^{-1} mmHg^{-1}$	Monod et al. (1965)
M	transfer factor for carbon oxygen across the capillary-alveolar membrane	$23.86 ml \cdot mmHg^{-1}$	Chakraborty et al. (2004)

compliance and narrowing vessel radius. The subject-specific tidal volume, cardiac output, oxygen consumption (VO_2) and carbon dioxide consumption (VCO_2) were estimated based on the patient's individual information. Data from PFTs (introduced in Section 1.2.1) were used as boundary conditions to control the simulations.

Disease region labelling

The different tissue patterns classified by CALIPER were mapped to the individual airway/vessel trees of each subject. For each airway/vessel terminal node, the corresponding tissue pattern it belonged to (surrounded by) was extracted (through finding the tissue pattern of the closest voxel to the node), so that each terminal node can be indexed to a particular tissue pattern. The percentage distribution of each tissue pattern against gravitational height (cranio-caudal axis) quantified in Chapter 4 was also used in the labelling. If the initial labelled amount of disease nodes was less than the cranio-caudal percentage, additional disease regions were added until the cranio-caudal distribution of disease matched the CALIPER classified data. Figure 1.3 shows the disease labelled airway nodes of one patient diagnosed with IPF. Table 1.3 lists the volume percentage of fibrosis (honeycomb + reticular + ground-glass) and emphysema classified by CALIPER software for each time point of these two patients.

Table 1.3: The volume percentage of CALIPER classified disease tissues for each time point of these two patients (%).

Patient No.	Time point	Honeycomb	Reticular	Ground-glass	Total fibrosis	Emphysema
Patient 1	Time point 1	< 1%	6.78	8.84	15.62	< 1%
	Time point 2	< 1%	4.13	13.62	17.77	< 1%
	Time point 3	< 1%	3.53	13.05	16.60	< 1%
Patient 2	Time point 1	< 1%	1.96	2.42	4.38	< 1%
	Time point 2	< 1%	4.12	8.58	12.72	< 1%

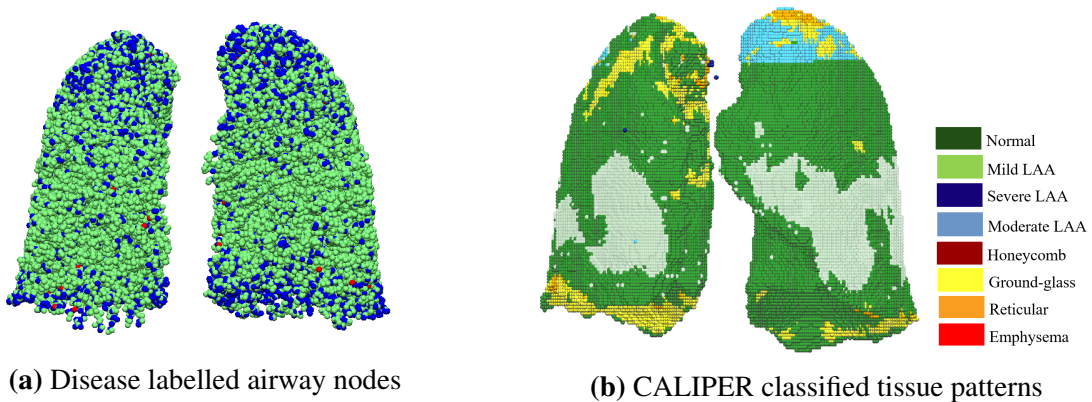


Figure 1.3: Disease labeled airway nodes. Green is classified as normal tissue, blue is fibrosis, and red is emphysema.

Deep inspiration model

To determine an appropriate total compliance for the IPF model, the model was required to predict the patient's forceful inhalation from FRC to TLC. Inhalation muscle pressure was assumed to be the same in normal and IPF, therefore an appropriate muscle pressure was estimated for the normal model and used in the IPF model. A deep inspiration model was constructed based on the ventilation model (introduced in Section 1.2.4) to simulate a deep inspiration from FRC to TLC. For simulation in the control models, the reference FRC volume (that is the patient-specific predicted normal volume as reference) from PFTs was used as an initial volume to start inspiration, and a subject-specific muscle pressure was solved to drive the lung expansion to the target reference TLC volume (the predicted TLC for the patient). Under the assumption that inspiratory muscle strength does not change with IPF disease (De Troyer and Yernault, 1980), the same driving pressure was used to simulate a deep inspiration in the corresponding IPF model. The IPF models started from their measured FRC. The modelling for IPF patients was divided into two separate stages:

1. The compliance of acini in labelled fibrosis regions (sum of honeycomb, reticular and ground-glass) was reduced to a very low value (less than 0.001 L/cmH₂O) to represent stiffness due to fibrosis. Then, inspiration was modelled under this initial fibrosis condition.

2. The deep inspiration volume for IPF models acquired in Step 1 was used as the target volume, and the tissue compliance of every acinar unit was scaled down together until the simulated inspiration volume can hit the target, then the corresponding scale factor of total tissue compliance was acquired.

Passive ventilation model

Time-averaged passive ventilation to each acinus over four breathing cycles was predicted using the previously described ventilation model. Acinar volumes in the control and IPF models were initialized to FRC, using the reference normal value and measured disease value, respectively. The scale factor for acinar tissue compliance identified in Step 2 (above) was applied in the simulation for the IPF patient. Patient-specific tidal volume was estimated based on the patient's weight, gender and height (Gilbert et al., 1972; Pelosi et al., 1998).

Perfusion model

The perfusion model introduced in Section 1.2.4 was used to estimate the distribution of blood. The individual age, weight, height and gender were used to predict the cardiac output for each patient (Brandfonbrener et al., 1955; Miyamura and HONDA, 1973; Stelfox et al., 2006), and the inlet and outlet pressure were adjusted in order to match the estimated cardiac output. Based on previous observations of reduced perfusion in regions of fibrosis (Crystal et al., 1976; Strickland et al., 1993; Plantier et al., 2018), the

blood vessel radius in the fibrosis labelled regions were narrowed for IPF models, so that the blood flow would be reduced to the abnormal tissue.

Gas exchange model

The gas transport and exchange were simulated using the gas exchange model introduced in Section 1.2.4. The ventilation and perfusion distribution predicted by the ventilation and perfusion model were used as inputs in the normal and disease condition. Patient-specific oxygen consumption (VO_2) and carbon dioxide consumption (VCO_2) were estimated using the following equations (Kwan et al., 2004; Coelho-Ravagnani et al., 2013):

$$VO_2 = P_{VO_2} \times W, \quad (1.28)$$

$$VCO_2 = VO_2 \times 0.8, \quad (1.29)$$

where P_{VO_2} is the oxygen consumption at rest ($P_{VO_2} = 2.84 \pm 0.34 \text{ml/kg}^{-1}/\text{min}^{-1}$ for male and $P_{VO_2} = 2.82 \pm 0.37 \text{ml/kg}^{-1}/\text{min}^{-1}$ for female), and W is the weight of the patient (kg).

Using the patient-specific (or control-specific) tidal volume and dead space, and patient- (or control-) specific distribution of \dot{V} and \dot{Q} , the partial pressure of oxygen in alveolar (P_AO_2) and in arterial blood (P_aO_2) can be predicted using the Kapitan & Hempleman gas transfer model (Kapitan and Hempleman, 1986).

1.3 Results

1.3.1 Construction of lung lobe geometry

Table 1.4 lists the age, BMI and functional measures used for normal control lung shape prediction for one patient with IPF. The values for FVC, TLC, RV/TLC, and DLCO were predicted reference values from the patient's individual information. Figure 1.4 presents the lung mesh of the IPF patient and its corresponding predicted control lung mesh for the matching normal.

The lobe volume proportions for IPF lung meshes and predicted control meshes are shown in Table 1.5. As discussed in Chapter 4, Section ??, the shape change in IPF usually relates to a relatively larger anterior-posterior diameter and smaller height of the lung. The IPF lung has a lower average volume proportion for the left lower lobe and right lower lobe compared with normal older subjects. The results illustrated in Figure 1.4 and Table 1.5 are consistent with these previous findings, with the predicted lung mesh for normal controls showing a "thinner" and "elongated" shape and lower average volume of left and right lower lobes compared with the IPF mesh generated from CT imaging.

Table 1.4: Predicted reference values used as input to predict a shape model for a normal control.

Parameters	Age	BMI	FVC(L)	TLC(L)	RV/TLC	DLCO(mL/mmHg/min)
Values	82	32.77	3.87	7.22	46	25.1

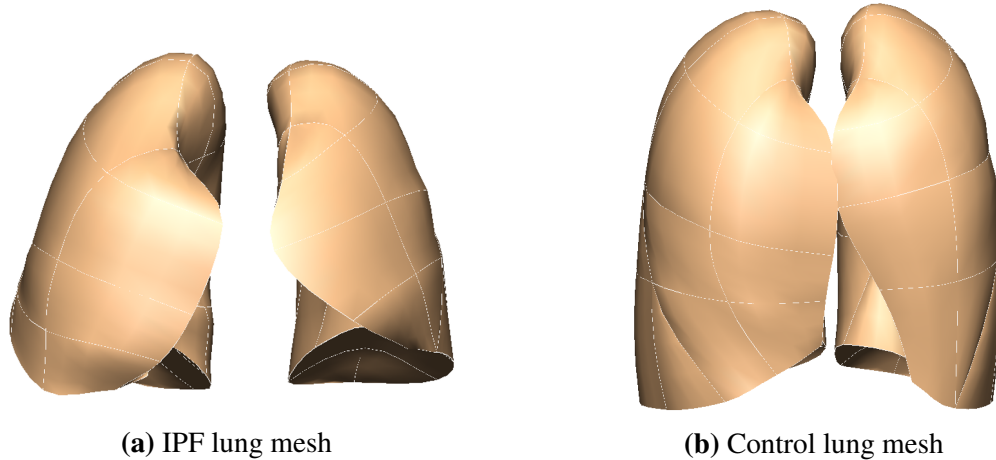


Figure 1.4: Lung mesh for IPF subject and the predicted lung mesh for a normal control with same characteristics. (a) IPF lung mesh generated from CT imaging of a patient with IPF. (b) Control mesh predicted using the reference values for the same patient.

1.3.2 Construction of airway/vasculature geometry

Airway tree

Figure 1.5 illustrates the generated airway trees of one IPF patient and its corresponding predicted airway tree for the control.

Table 1.5: Average lobe volume proportion of IPF lung mesh and predicted control lung mesh.

Patient No.	Time point	LLL		LUL		RLL		RML		RUL	
		Control	IPF								
Patient 1	Time point 1	0.249	0.253	0.222	0.287	0.277	0.214	0.079	0.144	0.173	0.102
	Time point 2	0.248	0.257	0.222	0.287	0.277	0.211	0.079	0.144	0.174	0.102
	Time point 3	0.249	0.265	0.221	0.286	0.278	0.187	0.079	0.143	0.172	0.119
Patient 2	Time point 1	0.231	0.194	0.238	0.287	0.262	0.213	0.081	0.105	0.188	0.201
	Time point 2	0.234	0.186	0.236	0.302	0.265	0.201	0.080	0.112	0.186	0.199
Average		0.242	0.231	0.228	0.290	0.272	0.205	0.078	0.130	0.179	0.144

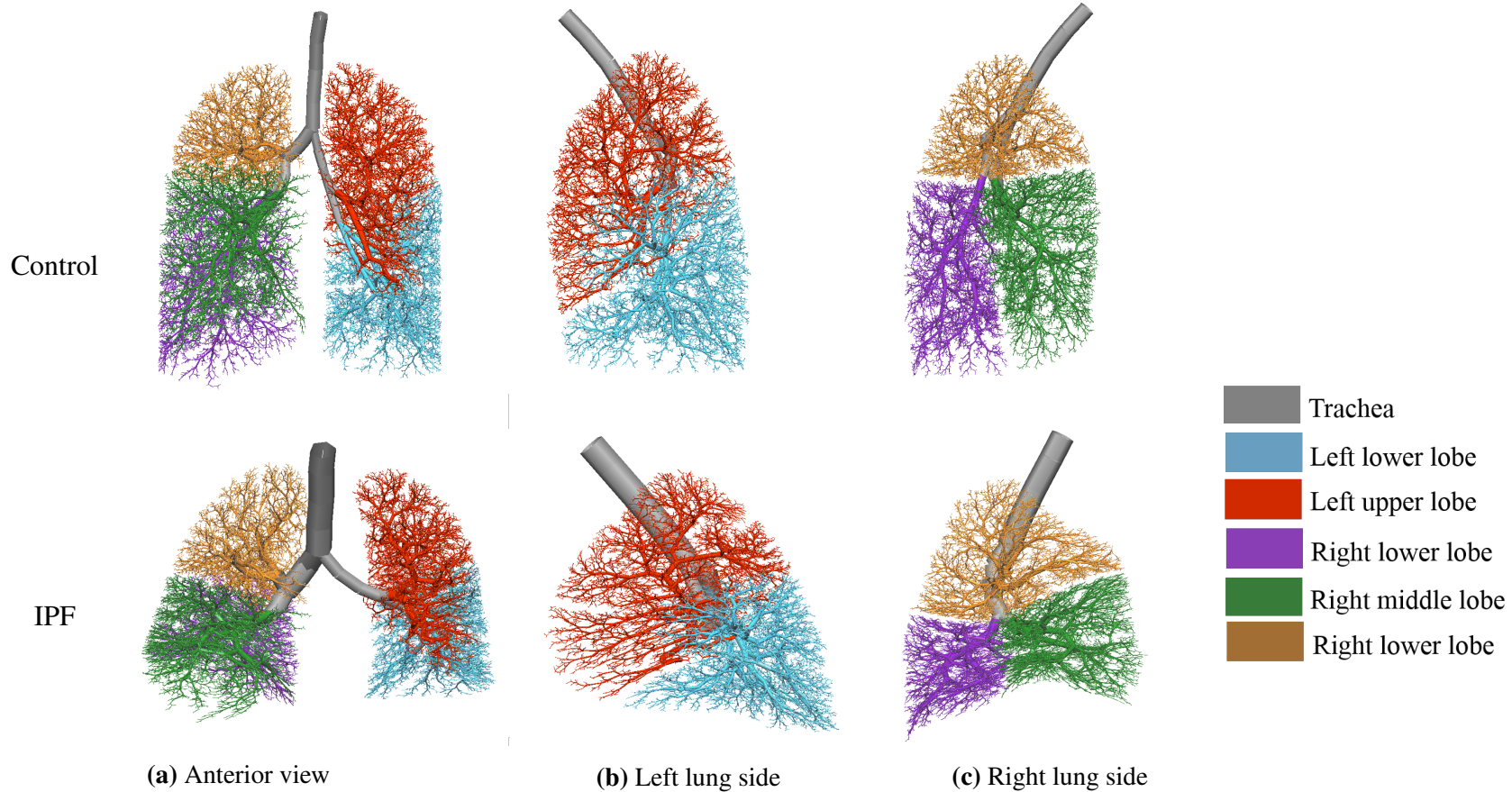


Figure 1.5: Generated normal control airway tree (top row) and IPF airway tree (bottom row) for one patient diagnosed with IPF. (a) Anterior view. (b) Left lung side. (c) Right lung side.

From Figure 1.5, it can be seen that compared with the control airway tree, the IPF airway tree has a larger trachea radius (which is associated with the dilation of the conducting airway in the IPF lung), a relatively smaller lower lobe and a larger anterior-posterior diameter with respect to the crano-caudal length. These features are consistent with the SSM based analysis result of IPF lung shape in Chapter 4.

Vascular tree

The generated IPF and control artery trees are shown in Figure 1.6. Table 1.6 lists the parameters used for generating the airway tree. Table 1.7 lists the parameters for generating vessel trees.

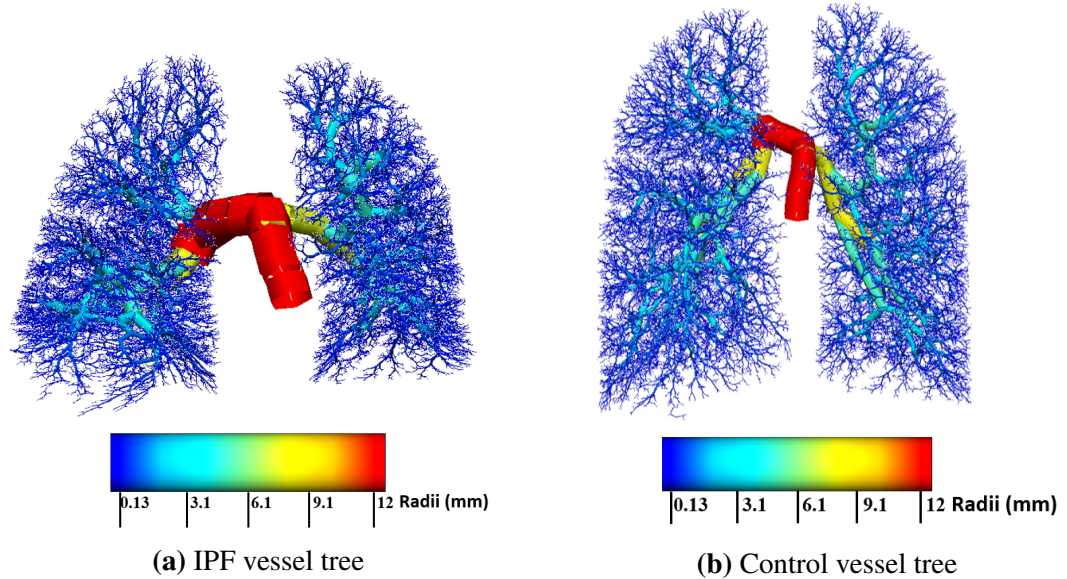


Figure 1.6: Generated geometry of the vessel trees. (a) IPF vessel tree. (b) Control vessel tree. The radius of branches are visualized as shown by the colour bars.

Table 1.6: Parameters of control and IPF airway tree

Patient No.	Time point	Trachea radius (mm)		Horsfield diameter ratio(R_dH)		Terminal radius (mm)		Airway volume (ml)	
		Normal	IPF	Normal	IPF	Normal	IPF	Normal	IPF
Patient 1	Time point 1	6.00	8.81	1.14	1.16	0.20	0.18	76.14	99.80
	Time point 2	6.00	9.82	1.14	1.17	0.20	0.18	75.53	123.87
	Time point 3	6.00	10.03	1.14	1.16	0.20	0.18	74.17	134.84
Patient 2	Time point 1	6.50	9.678	1.14	1.16	0.20	0.18	87.70	110.99
	Time point 2	6.50	8.71	1.14	1.15	0.20	0.18	88.85	111.15

Table 1.7: Parameters of control and IPF vessel tree

Patient No.	Time point	Main artery radius (mm)		Artery R_dS		Main vein radius (mm)		Vein R_dS	
		Normal	IPF	Normal	IPF	Normal	IPF	Normal	IPF
Patient 1	Time point 1	7.69	11.28	1.45	1.51	9.17	14.66	1.48	1.54
	Time point 2	7.69	12.58	1.45	1.52	9.17	16.75	1.48	1.56
	Time point 3	7.69	12.86	1.45	1.52	9.17	17.20	1.48	1.56
Patient 2	Time point 1	8.33	12.40	1.52	1.58	11.18	18.38	1.57	1.65
	Time point 2	8.33	11.16	1.52	1.57	11.18	16.11	1.57	1.63

1.3.3 Deep inspiration modelling

Table 1.8 lists the deep inspiration volumes (from FRC to TLC) for the reference values, simulated, and measured values (from the PFT report). In Table 1.8, the simulated inspiration volume (with CT-based abnormality labelling) at all time points for the two patients are higher than the measured values. That is, loss of compliance in the abnormal (fibrosis) regions on the volumetric CT is not sufficient to explain the reduction in inspiration volume from FRC to TLC in the model, except at time point 3 in patient 1.

Table 1.8: Reference normal, simulated and PFT measured inspiration volume.

Patient No.	Time point	Ref. normal volume	Simulated volume	Measured volume
Patient 1	Time point 1	1.93	1.26	1.16
	Time point 2	1.93	1.27	1.12
	Time point 3	1.84	1.15	1.14
Patient 2	Time point 1	3.4	2.58	2.37
	Time point 2	3.36	2.37	1.93

Additional "fibrosis" was added to the CALIPER classified "normal" tissues until the modelled inspiration volume matched the measured one (as in the last column of Table 1.8). The percentages of CT-based fibrosis (CALIPER classified) and PFT-based fibrosis (CALIPER classified + additional labelled) are listed in Table 1.9.

Table 1.9: Percentage of CT-based fibrosis from CALIPER classification and PFT-based fibrosis (CT-based plus additional fibrosis required to limit inspiration from FRC to TLC).

Patient No.	Time point	CT-based fibrosis (%)	PFT-based fibrosis (%)
Patient 1	Time point 1	17.6	23.7
	Time point 2	18.9	28.9
	Time point 3	22.1	22.9
Patient 2	Time point 1	4.3	11.9
	Time point 2	12.5	29.1

The total lung compliance (including the chest wall compliance in parallel with the

lung) predicted from control, CT-based and PFT-based models for each time point are presented in Table 1.10. From Table 1.9 and 1.10, the total lung compliance experiences a drop with increasing fibrosis percentage.

Table 1.10: Values of total lung compliance (L/cmH₂O) of normal control, CT-based and PFT-based modelling results.

Patient No.	Time point	Control	CT-based	PFT-based
Patient 1	Time point 1	0.108	0.070	0.064
	Time point 2	0.108	0.070	0.060
	Time point 3	0.106	0.067	0.066
Patient 2	Time point 1	0.120	0.099	0.089
	Time point 2	0.120	0.090	0.069

1.3.4 Perfusion modelling

Table 1.11 lists the mean pulmonary artery pressure (mPAP), pulmonary vascular resistance (PVR) and pulmonary blood vessel (PVV) of control, CT-based and PFT-based models for each time point of these two patients. From the table, the CT-based model has a consistently lower mPAP value compared with the PFT-based model which has more "fibrosis" constriction. That is, there is an increase in mPAP when occluding more small vessels in IPF lungs. For PVV, disease models (both CT-based and PFT-based) have a higher value than the normal control model, but most of the increase in PVV probably comes from the larger pulmonary artery size set for disease vessel models. In spite of this, the PVV of the PFT-based model is also slightly higher compared with the CT-based model. This result is consistent with the observation of Jacob et al. (2016b,a), which indicated that an increase in PVV can be seen in lungs with more advanced fibrosis. Moreover, when comparing PFT model with CT model, it can be seen a larger value of PVR, which leads to a dilation of arteries and an increase in PVV.

Table 1.11: Values of mPAP (mmHg), PVR (MPa·/mm³) and PVV (ml) of normal control, CT-based and PFT-based modelling results.

Patient No.	Time point	mPAP			PVR			PVV		
		Control	CT-based	PFT-based	Control	CT-based	PFT-based	Control	CT-based	PFT-based
Patient 1	Time point 1	14.46	14.68	14.93	15.91	16.59	17.31	260.16	410.43	411.30
	Time point 2	14.51	14.54	14.92	15.23	15.36	16.48	260.99	550.82	552.57
	Time point 3	14.66	14.43	14.47	17.90	17.40	17.52	272.38	583.91	584.11
Patient 2	Time point 1	14.96	14.59	14.93	12.97	12.35	12.92	509.49	886.57	889.38
	Time point 2	14.66	15.10	16.02	12.64	13.36	14.88	515.30	798.78	804.67

1.3.5 Gas exchange model

Figure 1.7 illustrates the distribution of control, CT-based and PFT-based simulated V/Q ratio and arterial oxygen at one time point for one IPF patient. The figures are shown with V/Q plotted on a logarithmic scale, which is consistent with the presentation of V/Q measurements using the multiple inert gas elimination technique (MIGET). From the results, the simulation for the control model (the first row) predicts a normal V/Q ratio distribution with PaO_2 of 89.33 mmHg; this slightly low PaO_2 is typical for the normal older adult. In the control model, most of the alveoli are in the $P_a\text{O}_2$ range of 80-100 mmHg. The model labelled with CT-based fibrosis predicts a characteristic (for IPF) bimodal V/Q distribution (the second row), and PaO_2 considerably decreased (71.63 mmHg) from the control. The higher proportion of alveoli appears at high $P_a\text{O}_2$ because of the high \dot{V} compared with \dot{Q} . It can be observed that about 10% of alveoli have $P_c\text{O}_2$ lower than 63 mmHg which has a net effect of the reduction in total $P_a\text{O}_2$. Also, in the CT-based model, there are more low $P_c\text{O}_2$ acinus units with relatively high perfusion. A slight shift to the left hand side is observed for the highest peak of the V/Q ratio curve compared with the control model. The smaller peak of the V/Q ratio appears around $\text{V}/\text{Q} = 5$ (larger than 1), as there is a decrease in perfusion in fibrotic regions due to the narrowed vessel radius. The model with additional fibrosis (with appropriate patient-specific inspiration from FRC to TLC) predicts further decrease in PaO_2 to 67.85 mmHg. There is an increase in the proportion of well-perfused but less ventilated units, which leads to more alveoli at low $P_c\text{O}_2$. Meanwhile, the proportion of ventilation also increases at very high $P_c\text{O}_2$ units in the PFT-based model compared with the other two models.

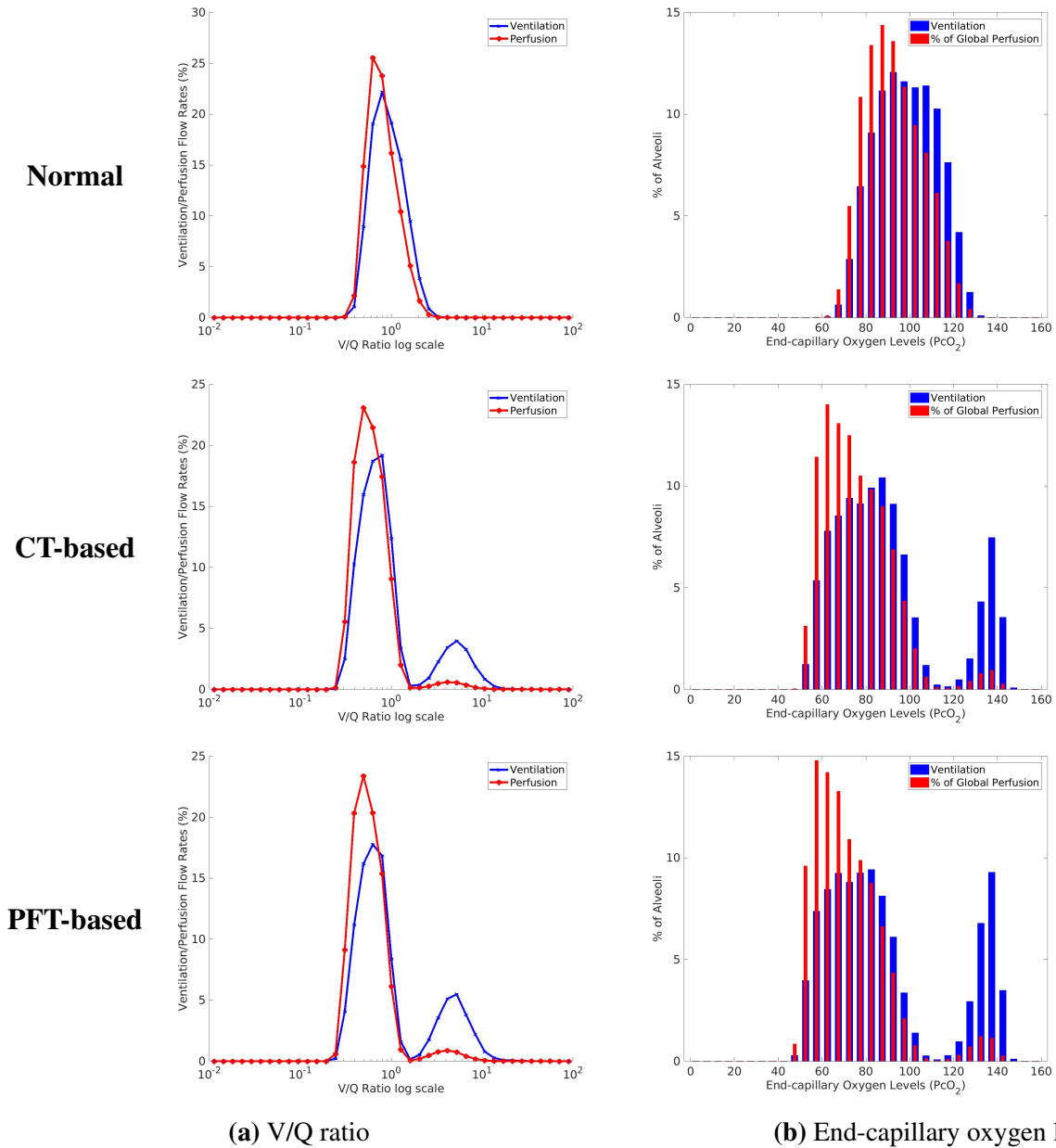


Figure 1.7: V/Q ratio distribution and end-capillary oxygen distribution of control, CT-based and PFT-based simulation result at one time point for one patient diagnosed with IPF). (a) V and Q with respect to V/Q ratio. (b) Distribution of end-capillary oxygen levels amongst alveoli.

Figure 1.8 shows the \dot{V} , \dot{Q} and V/Q ratio distributions against lung height (cranio-caudal axis) simulated in the control, CT-based and PFT-based models. For the upright models, \dot{V} is higher in the lung base than apex (Figure 1.8a). The main difference between the control and fibrosis models is a left-wards shift of the \dot{V} curves because of lower total ventilation. The CT- and PFT-based models have very similar \dot{V} . Differences in \dot{Q} are mainly in the basal part of the lung, where more fibrosis appears in the fibrosis models. The two fibrosis models have much higher variability of \dot{Q} within iso-gravitational slices (the error bars in Figure 1.8a and 1.8b) than the control model, particularly in the basal region. For the control model simulation, V/Q ratio is ~ 1 , with a slight increase moving apically.

The measured DLCO values for each time point of these two patients, and the values of PaO_2 and PaCO_2 for control, CT-based and PFT-based models for each time point are listed in Table 1.12. For CT-based and PFT-based simulation, PaO_2 experiences an overall decrease over time for both of these two patients, corresponding to the gradual increase of fibrosis. The reduction of PaO_2 and $P(A - a)\text{O}_2$ predicted by the PFT-based model follows the reduction in measured DLCO (and $P(A - a)\text{O}_2$, which has an opposite trend), with the first patient decreasing from time point 1 to time point 2 but slightly increasing from time point 2 to time point 3, and the second patient decreasing from time point 1 to time point 2. MIGET plots of V/Q ratio and arterial oxygen distribution, plots of cranio-caudal distribution of V , Q and V/Q ratio for other subjects and time points can be found in Appendix ??.

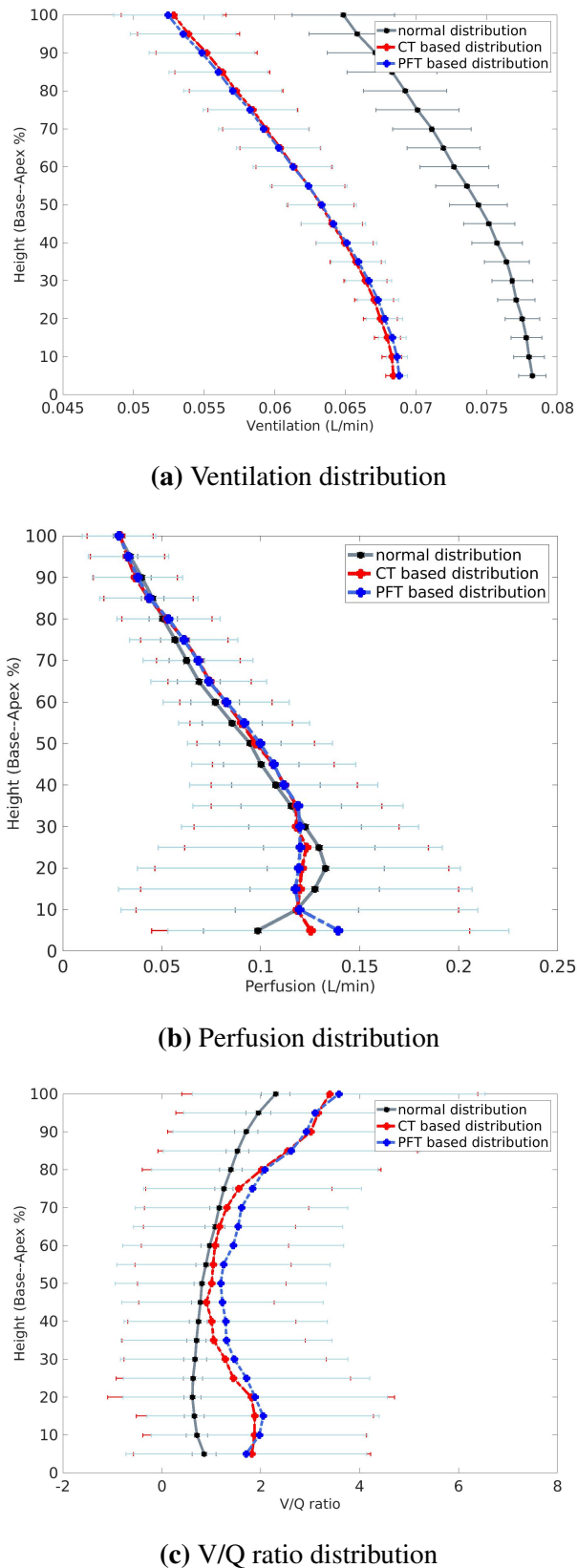


Figure 1.8: Ventilation, perfusion and V/Q ratio distribution against lung height (cranio-caudal axis). (a) Ventilation distribution against lung height. (b) Perfusion distribution against lung height. (c) V/Q ratio distribution against lung height.

Table 1.12: Measured DLCO (mL/mmHg/min) for each time point, and values of PaO₂ (mmHg), PaCO₂ (mmHg) and P(A – a)O₂ (mmHg) of normal control, CT-based and PFT-based modelling results.

Patient No.	Time point	DLCO	PaO ₂			PaCO ₂			P(A – a)O ₂		
			Control	CT-based	PFT-based	Control	CT-based	PFT-based	Control	CT-based	PFT-based
Patient 1	Time point 1	11.8	89.33	71.63	67.85	41.87	52.73	53.97	8.59	17.09	20.79
	Time point 2	9.8	95.37	64.56	58.72	37.81	57.48	59.58	7.69	18.13	23.87
	Time point 3	10.12	87.92	60.43	60.00	42.76	59.83	59.97	9.01	20.85	21.29
Patient 2	Time point 1	16.20	92.31	88.52	85.13	39.80	41.74	42.86	9.90	10.06	13.35
	Time point 2	14.50	91.72	83.70	75.35	39.09	43.77	46.76	9.75	14.29	22.94

1.4 Discussion

SSM based lung shape prediction provides a way to compare lung function of IPF patient with older normal people

In this chapter, an SSM was used to make a prediction of older normal lung shape for each patient. The SSM based lung shape prediction provides a way to make a comparison of the lung function between a patient-specific lung and its corresponding normal equivalent. The patient-specific shape prediction was achieved based on the patient's individual information which shows significant correlations with older normal lung shape, therefore the estimated lung shape is able to represent the statistical lung shape of older normal people as a control group. Through modelling the airway/vessel tree and lung function with the predicted normal lung mesh, it is possible to quantitatively describe the change of respiratory geometry in IPF lung, the decline of lung function, the severity of disease and the prediction of progression. This could be a promising direction for clinical applications in the future.

Volumetric CT imaging may not provide sufficient information to explain the stiffness of the IPF lung

The computational modelling in this chapter suggests that radiologically-identified tissue abnormalities from volumetric CT imaging may be not sufficient to explain the increase in lung stiffness and the decline of lung function in IPF patients. Under the assumption that inspiratory muscle pressure does not change in IPF, ascribing only "abnormal" tissue to be highly stiffened could not fully explain the reduction in TLC-FRC volume. Additional tissue (up to 10% in patient 1 and 17% in patient 2) was required to be stiffened to achieve a correct prediction of volume change from FRC to TLC. The

proportion of fibrosis increased in both patients over time, and the additional fibrosis in the PFT model increased this further except for time point 3 in patient 1, where no "additional" fibrosis was needed. It is reasonable to expect that tissue with normal appearance on CT has already undergoing remodelling that affects its function. Extension of this method and validation in a larger number of subjects could provide an estimate of the proportion of visually normal but functionally abnormal tissue. V/Q mismatch (impaired gas exchange) is present in CT-based abnormal tissue as well as in regions that are classified as 'normal'. Additional V/Q mismatch emerges in the PFT-based model, which results in a reduction in P_aO_2 and increase in P_aCO_2 . Blood gas data was not available for any subjects in this thesis to compare with the model predictions; however, DLCO reduced over time and was consistent with the model's prediction of gas exchange impairment.

The predicted ventilation, perfusion and gas exchange distribution can be explained by the background knowledge of IPF

The physiological alterations in IPF (discussed in Chapter 2, Section ??) are supportive of the modelling results. First, it has been found that IPF disease often results in reduction in total lung compliance (an increase in lung tissue stiffness), and the alterations of total lung compliance in IPF patients appear to be strongly correlated with the degree of lung fibrosis (Fulmer et al., 1979; Plantier et al., 2018). As should be expected, the total compliance predicted by the ventilation (deep inspiration) model (Table 1.9 and 1.10) decreases with more fibrosis added into the model lung tissues. Second, although the fibrotic tissue is associated with a reduced number of blood vessels (Cosgrove et al., 2004; Ebina et al., 2004), Jacob et al. (2016b,a) has demonstrated that pulmonary vessel volume (PVV) increases with fibrosis, and can be used as an independent predictor

of mortality. Similarly, the predicted PVV in the PFT-based model is higher than the CT-based model, despite having additional vessel occlusions. The larger PVR in the PFT-based model results in slightly higher mPAP which distends the arteries and increases PVV. It should be noted that the assumed tissue tethering pressure (from tissue to blood vessels) was the same in both models. If this were increased in the PFT-based model, it would further increase PVV. In addition, in the perfusion model, the predicted PVV of disease models are higher than the normal control model, but this might be mainly caused by the larger vessel radius set for the disease vessel geometry. Third, the predicted P_aO_2 (which decreases in IPF lung model) and $P_{A-a}O_2$ (increases in the IPF lung model) from the gas exchange model presents a consistent trend with the change of measured DLCO (from PFTs) over time. DLCO is an important index to measure the gas exchange function of the lung, therefore while the simulated P_aO_2 and $P_{A-a}O_2$ cannot be compared directly against data for these subjects, it is reassuring that the model gas exchange follows the DLCO trend. Collection of blood gas data is not standard during lung function testing, whereas measurement of DLCO is. It would therefore be appropriate in future studies to model DLCO (as a surrogate of gas exchange) and compare directly against data. The preliminary outcomes of the modelling framework demonstrated in this chapter suggest that a model-based approach that combines simulation of abnormal mechanics (from FRC to TLC) and gas exchange could be used to estimate the amount of abnormally-functioning lung tissue that appears radiologically normal.

Limitations of modelling procedure

There are some limitations of the modelling procedure introduced in this chapter. First, in the IPF lung, there is a dilation in trachea, but a constriction in small airway. In

this chapter, the trachea radius of normal lung was scaled from the trachea radius of the IPF lung using a statistically measured ratio which represents the conducting airway volume difference between normal and IPF. The main limitation of this method is that the measured ratio may be not accurate enough for all the subjects even though the standard deviation has been taken into consideration here. A potential approach in future work could be to use the change of dead space to tidal volume ratio in IPF lung in the construction of the airway geometry.

Second, regions of tissue classified as the emphysema or low attenuation area (LAA) were not taken into consideration in this model. Although emphysema classified by CAPLIPER only covers a small proportion of the lung (usually less than 1%), it is believed to have an impact on the deterioration of lung function together with fibrosis in IPF (Cottin et al., 2005; King Jr et al., 2011; Lin and Jiang, 2015). LAA (mild, moderate and severe) can account for a sizable proportion of the lung; both emphysema and LAA are associated with air trapping at the end of inspiration (Slebos et al., 2015; Hoessein and De Jong, 2017), which will influence the lung volume at FRC and the change of tissue compliance during breathing. Therefore emphysema and LAA should be accounted for in future extensions of this work.

Third, for some end-stage subjects with a large proportion of fibrotic lesion and a small constricted FRC volume, a larger driving pressure may be needed to drive the expansion of the stiffer lung to TLC, because the deep inspiration volume won't be estimated accurately with a "normal" driving pressure. For future studies, this could require explicitly modelling the chest wall in normal and IPF subjects, to understand how chest wall shape change affects chest wall mechanics and the pressures developed during deep inspiration.

1.5 Summary

In this chapter, a preliminary patient-specific computational modelling method was developed to investigate the association between lung structure and lung function in IPF patients. In order to make a comparison between IPF patients and older normal people, an SSM was used to make a prediction of the lung shape of an equivalent older normal for each patient, and the V/Q distribution and gas exchange were then simulated in normal and IPF conditions, respectively, with CALIPER tissue classification data and PFT data as input. The results show that the computational model can predict a reasonable level of abnormality in ventilation, perfusion and gas exchange in the IPF lung, and suggests a difference of lung function between IPF and older normal people. Moreover, the model results suggest based tissue abnormalities do not fully explain the change in lung function in IPF. These preliminary results suggests that a model-based approach could be developed to estimate the amount of "normal" appearing tissue with abnormal function, by considering both lung mechanics (expansion from FRC to TLC) and gas exchange.

List of References

- Aho, K., Derryberry, D., and Peterson, T. (2014). Model selection for ecologists: the worldviews of aic and bic. *Ecology*, 95(3):631–636. [Cited on page 12.]
- Arora, N. S. and Rochester, D. F. (1982). Respiratory muscle strength and maximal voluntary ventilation in undernourished patients. *American Review of Respiratory Disease*, 126(1):5–8. [Cited on page 5.]
- Brandfonbrener, M., Landowne, M., and Shock, N. W. (1955). Changes in cardiac output with age. *Circulation*, 12(4):557–566. [Cited on page 31.]
- Brandstetter, R. D. and Kazemi, H. (1983). Aging and the respiratory system. *Medical Clinics of North America*, 67(2):419–431. [Cited on page 6.]
- Breatnach, E., Abbott, G. C., and Fraser, R. G. (1984). Dimensions of the normal human trachea. *American Journal of Roentgenology*, 142(5):903–906. [Cited on page 17.]
- Butler, C. and Kleinerman, J. (1970). Capillary density: alveolar diameter, a morphometric approach to ventilation and perfusion. *American Review of Respiratory Disease*, 102(6):886–894. [Cited on page 7.]
- Chakraborty, S., Balakotaiah, V., and Bidani, A. (2004). Diffusing capacity reexamined: relative roles of diffusion and chemical reaction in red cell uptake of o₂, co, co₂, and no. *Journal of applied physiology*, 97(6):2284–2302. [Cited on pages 27 and 28.]

- Clark, A., Milne, D., Wilsher, M., Burrowes, K., Bajaj, M., and Tawhai, M. (2014). Lack of functional information explains the poor performance of ‘clot load scores’ at predicting outcome in acute pulmonary embolism. *Respiratory physiology & neurobiology*, 190:1–13. [Cited on pages 19 and 24.]
- Clark, A. R., Burrowes, K. S., and Tawhai, M. H. (2010). Contribution of serial and parallel microperfusion to spatial variability in pulmonary inter-and intra-acinar blood flow. *Journal of applied physiology*, 108(5):1116–1126. [Cited on pages 17, 19, and 28.]
- Clark, A. R., Tawhai, M. H., Hoffman, E. A., and Burrowes, K. S. (2011). The interdependent contributions of gravitational and structural features to perfusion distribution in a multiscale model of the pulmonary circulation. *Journal of applied physiology*, 110(4):943–955. [Cited on pages 17, 19, 21, and 27.]
- Coelho-Ravagnani, C. d. F., Melo, F. C. L., Ravagnani, F. C., Burini, F. H. P., and Burini, R. C. (2013). Estimation of metabolic equivalent (met) of an exercise protocol based on indirect calorimetry. *Revista Brasileira de Medicina do Esporte*, 19(2):134–138. [Cited on page 32.]
- Cosgrove, G. P., Brown, K. K., Schiemann, W. P., Serls, A. E., Parr, J. E., Geraci, M. W., Schwarz, M. I., Cool, C. D., and Worthen, G. S. (2004). Pigment epithelium-derived factor in idiopathic pulmonary fibrosis: a role in aberrant angiogenesis. *American journal of respiratory and critical care medicine*, 170(3):242–251. [Cited on page 48.]
- Cottin, V., Nunes, H., Brillet, P., Delaval, P., Devouassoux, G., Tillie-Leblond, I., Israel-Biet, D., Valeyre, D., Cordier, J., et al. (2005). Combined pulmonary fibrosis and emphysema: a distinct underrecognised entity. *European Respiratory Journal*, 26(4):586–593. [Cited on page 50.]
- Crapo, R. (1993). The aging lung. *Lung biology in health and disease*, 63:1–25. [Cited on pages 3 and 6.]

- Crystal, R. G., Fulmer, J. D., Roberts, W. C., Moss, M. L., Line, B. R., and Reynolds, H. Y. (1976). Idiopathic pulmonary fibrosis: clinical, histologic, radiographic, physiologic, scintigraphic, cytologic, and biochemical aspects. *Annals of internal medicine*, 85(6):769–788. [Cited on pages 16 and 31.]
- De Troyer, A. and Yernault, J.-C. (1980). Inspiratory muscle force in normal subjects and patients with interstitial lung disease. *Thorax*, 35(2):92–100. [Cited on page 30.]
- Ebina, M., Shimizukawa, M., Shibata, N., Kimura, Y., Suzuki, T., Endo, M., Sasano, H., Kondo, T., and Nukiwa, T. (2004). Heterogeneous increase in cd34-positive alveolar capillaries in idiopathic pulmonary fibrosis. *American journal of respiratory and critical care medicine*, 169(11):1203–1208. [Cited on page 48.]
- Fulmer, J., Roberts, W., von Gal, E. R., and Crystal, R. (1979). Morphologic-physiologic correlates of the severity of fibrosis and degree of cellularity in idiopathic pulmonary fibrosis. *The Journal of clinical investigation*, 63(4):665–676. [Cited on page 48.]
- Fung, Y. and Sabin, S. (1969). Theory of sheet flow in lung alveoli. *Journal of Applied Physiology*, 26(4):472–488. [Cited on pages 23 and 28.]
- Fung, Y.-c. (2013). Biomechanics: circulation. Springer Science & Business Media. [Cited on page 28.]
- Gilbert, R., Auchincloss Jr, J., Brodsky, J., and Boden, W. a. (1972). Changes in tidal volume, frequency, and ventilation induced by their measurement. *Journal of Applied Physiology*, 33(2):252–254. [Cited on page 31.]
- Glazier, J., Hughes, J., Maloney, J., and West, J. (1969). Measurements of capillary dimensions and blood volume in rapidly frozen lungs. *Journal of Applied Physiology*, 26(1):65–76. [Cited on page 24.]

- Guenard, H. and Marthan, R. (1996). Pulmonary gas exchange in elderly subjects. *European Respiratory Journal*, 9(12):2573–2577. [Cited on page 7.]
- Haefeli-Bleuer, B. and Weibel, E. R. (1988). Morphometry of the human pulmonary acinus. *The Anatomical Record*, 220(4):401–414. [Cited on page 15.]
- Hoesein, F. A. M. and De Jong, P. A. (2017). Air trapping on computed tomography: regional versus diffuse. [Cited on page 50.]
- Holland, J., Milic-Emili, J., Macklem, P., and Bates, D. (1968). Regional distribution of pulmonary ventilation and perfusion in elderly subjects. *The Journal of clinical investigation*, 47(1):81–92. [Cited on page 7.]
- Horsfield, K. (1978). Morphometry of the small pulmonary arteries in man. *Circulation research*, 42(5):593–597. [Cited on page 18.]
- Horsfield, K., Dart, G., Olson, D. E., Filley, G. F., and Cumming, G. (1971). Models of the human bronchial tree. *Journal of applied physiology*, 31(2):207–217. [Cited on page 18.]
- Horsfield, K. and Gordon, W. (1981). Morphometry of pulmonary veins in man. *Lung*, 159(1):211–218. [Cited on page 18.]
- Horsfield, K., Relea, F. G., and Gumming, G. (1976). Diameter, length and branching ratios in the bronchial tree. *Respiration physiology*, 26(3):351–356. [Cited on page 16.]
- Hsia, C. C., Hyde, D. M., and Weibel, E. R. (2016). Lung structure and the intrinsic challenges of gas exchange. *Comprehensive Physiology*, 6(2):827. [Cited on page 17.]
- Huang, W., Yen, R., McLaurine, M., and Bledsoe, G. (1996). Morphometry of the human pulmonary vasculature. *Journal of applied physiology*, 81(5):2123–2133. [Cited on page 18.]

- Jacob, J., Bartholmai, B. J., Rajagopalan, S., Brun, A. L., Egashira, R., Karwoski, R., Kokosi, M., Wells, A. U., and Hansell, D. M. (2016a). Evaluation of computer-based computer tomography stratification against outcome models in connective tissue disease-related interstitial lung disease: a patient outcome study. *Bmc Medicine*, 14(1):190. [Cited on pages 40 and 48.]
- Jacob, J., Bartholmai, B. J., Rajagopalan, S., Kokosi, M., Nair, A., Karwoski, R., Walsh, S. L., Wells, A. U., and Hansell, D. M. (2016b). Mortality prediction in ipf: evaluation of automated computer tomographic analysis with conventional severity measures. *European Respiratory Journal*, 49(1):ERJ-01011–2016. [Cited on pages 40 and 48.]
- Janssens, J.-P., Pache, J.-C., and Nicod, L. (1999). Physiological changes in respiratory function associated with ageing. *European Respiratory Journal*, 13(1):197–205. [Cited on pages 2, 3, 5, 6, and 7.]
- Kapitan, K. S. and Hempleman, S. C. (1986). Computer simulation of mammalian gas-exchange. *Computers in biology and medicine*, 16(2):91–101. [Cited on pages 24, 26, and 32.]
- King Jr, T. E., Pardo, A., and Selman, M. (2011). Idiopathic pulmonary fibrosis. *The Lancet*, 378(9807):1949–1961. [Cited on page 50.]
- Knudson, R. J., Slatin, R. C., Lebowitz, M. D., and Burrows, B. (1976). The maximal expiratory flow-volume curve: normal standards, variability, and effects of age. *American Review of Respiratory Disease*, 113(5):587–600. [Cited on page 6.]
- Krenz, G. S. and Dawson, C. A. (2003). Flow and pressure distributions in vascular networks consisting of distensible vessels. *American Journal of Physiology-Heart and Circulatory Physiology*, 284(6):H2192–H2203. [Cited on page 28.]
- Kwan, M., Woo, J., and Kwok, T. (2004). The standard oxygen consumption value equivalent to one metabolic equivalent (3.5 ml/min/kg) is not appropriate for elderly

- people. *International journal of food sciences and nutrition*, 55(3):179–182. [Cited on page 32.]
- Lalley, P. M. (2013). The aging respiratory system—pulmonary structure, function and neural control. *Respiratory physiology & neurobiology*, 187(3):199–210. [Cited on pages 3, 4, 5, 6, and 7.]
- Larsson, L. (1983). Histochemical characteristics of human skeletal muscle during aging. *Acta physiologica Scandinavica*, 117(3):469–471. [Cited on page 5.]
- Levitzky, M. G. (1984). Effects of aging on the respiratory system. *Physiologist*, 27(2):102–107. [Cited on page 7.]
- Lin, H. and Jiang, S. (2015). Combined pulmonary fibrosis and emphysema (cpfe): an entity different from emphysema or pulmonary fibrosis alone. *Journal of thoracic disease*, 7(4):767. [Cited on page 50.]
- McClaran, S., Babcock, M., Pegelow, D., Reddan, W., and Dempsey, J. (1995). Longitudinal effects of aging on lung function at rest and exercise in healthy active fit elderly adults. *Journal of Applied Physiology*, 78(5):1957–1968. [Cited on page 2.]
- Mittman, C., Edelman, N. H., Norris, A. H., and Shock, N. W. (1965). Relationship between chest wall and pulmonary compliance and age. *Journal of Applied Physiology*, 20(6):1211–1216. [Cited on pages 2 and 5.]
- Miyamura, M. and HONDA, Y. (1973). Maximum cardiac output related to sex and age. *The Japanese journal of physiology*, 23(6):645–656. [Cited on page 31.]
- Monod, J., Wyman, J., and Changeux, J.-P. (1965). On the nature of allosteric transitions: a plausible model. *Biol*, 12:228–113. [Cited on pages 25, 26, and 28.]
- Murray, J. F. (1986). *The normal lung: the basis for diagnosis and treatment of pulmonary disease*. WB Saunders Company. [Cited on pages 3 and 7.]

- Osanlouy, M. (2018). Statistical Shape Analysis to Quantify Lung Structure-Function Relationships over the Adult Lifespan. PhD thesis, University of Auckland. [Cited on pages 8 and 11.]
- Paoletti, P., Viegi, G., Pistelli, G., Di Pede, F., Fazzi, P., Polato, R., Saetta, M., Zambon, R., Carli, G., Giuntini, C., et al. (1985). Reference equations for the single-breath diffusing capacity: a cross-sectional analysis and effect of body size and age. *American Review of Respiratory Disease*, 132(4):806–813. [Cited on page 7.]
- Pedley, T., Schroter, R., and Sudlow, M. (1970). Energy losses and pressure drop in models of human airways. *Respiration physiology*, 9(3):371–386. [Cited on pages 20 and 28.]
- Pelosi, P., Croci, M., Ravagnan, I., Tredici, S., Pedoto, A., Lissoni, A., and Gattinoni, L. (1998). The effects of body mass on lung volumes, respiratory mechanics, and gas exchange during general anesthesia. *Anesthesia & Analgesia*, 87(3):654–660. [Cited on page 31.]
- Plantier, L., Cazes, A., Dinh-Xuan, A.-T., Bancal, C., Marchand-Adam, S., and Crestani, B. (2018). Physiology of the lung in idiopathic pulmonary fibrosis. *European Respiratory Review*, 27(147):170062. [Cited on pages 31 and 48.]
- Plantier, L., Debray, M.-P., Estellat, C., Flamant, M., Roy, C., Bancal, C., Borie, R., Israël-Biet, D., Mal, H., Crestani, B., et al. (2016). Increased volume of conducting airways in idiopathic pulmonary fibrosis is independent of disease severity: a volumetric capnography study. *Journal of breath research*, 10(1):016005. [Cited on pages 16 and 17.]
- Pollock, M. L., Mengelkoch, L. J., Graves, J. E., Lowenthal, D. T., Limacher, M. C., Foster, C., and Wilmore, J. H. (1997). Twenty-year follow-up of aerobic power and

- body composition of older track athletes. *Journal of Applied Physiology*, 82(5):1508–1516. [Cited on page 2.]
- Pries, A., Secomb, T., and Gaehtgens, P. (1996). Biophysical aspects of blood flow in the microvasculature. *Cardiovascular research*, 32(4):654–667. [Cited on page 28.]
- Slebos, D.-J., van Rikxoort, E. M., and van der Bijl, W. (2015). Air trapping in emphysema. *American journal of respiratory and critical care medicine*, 192(5):e45–e45. [Cited on page 50.]
- Smith, T. (1986). Respiratory effects of aging. In *Seminars in Anesthesia*, volume 5, pages 14–22. WB SAUNDERS CO INDEPENDENCE SQUARE WEST CURTIS CENTER, STE 300, PHILADELPHIA, PA 19106-3399. [Cited on page 2.]
- Sprung, J., Gajic, O., and Warner, D. O. (2006). age related alterations in respiratory function—anesthetic considerations. *Canadian journal of anesthesia*, 53(12):1244. [Cited on pages 2, 3, 4, 5, 6, and 7.]
- Stelfox, H. T., Ahmed, S. B., Ribeiro, R. A., Gettings, E. M., Pomerantsev, E., and Schmidt, U. (2006). Hemodynamic monitoring in obese patients: the impact of body mass index on cardiac output and stroke volume. *Critical care medicine*, 34(4):1243–1246. [Cited on page 31.]
- Strickland, N., Hughes, J., Hart, D., Myers, M., and Lavender, J. (1993). Cause of regional ventilation-perfusion mismatching in patients with idiopathic pulmonary fibrosis: a combined ct and scintigraphic study. *AJR. American journal of roentgenology*, 161(4):719–725. [Cited on page 31.]
- Swan, A. (2010). A multi-scale computational model of pulmonary gas exchange. PhD thesis, University of Auckland. [Cited on pages 2 and 27.]
- Swan, A. J., Clark, A. R., and Tawhai, M. H. (2012). A computational model of the

- topographic distribution of ventilation in healthy human lungs. *Journal of Theoretical Biology*, 300:222–231. [Cited on pages 19, 21, and 27.]
- Swan, A. J. and Tawhai, M. H. (2010). Evidence for minimal oxygen heterogeneity in the healthy human pulmonary acinus. *Journal of applied physiology*, 110(2):528–537. [Cited on page 27.]
- Tawhai, M. H., Hunter, P., Tschirren, J., Reinhardt, J., McLennan, G., and Hoffman, E. A. (2004). Ct-based geometry analysis and finite element models of the human and ovine bronchial tree. *Journal of applied physiology*, 97(6):2310–2321. [Cited on page 14.]
- Tawhai, M. H., Nash, M. P., Lin, C.-L., and Hoffman, E. A. (2009). Supine and prone differences in regional lung density and pleural pressure gradients in the human lung with constant shape. *Journal of Applied Physiology*, 107(3):912–920. [Cited on page 19.]
- Thurlbeck, W. M. and Angus, G. E. (1975). Growth and aging of the normal human lung. *Chest*, 67(2 Suppl):3S–6S. [Cited on page 7.]
- Turner, J. M., Mead, J., and Wohl, M. E. (1968). Elasticity of human lungs in relation to age. *Journal of applied physiology*, 25(6):664–671. [Cited on page 5.]
- Verbeken, E. K., Cauberghs, M., Mertens, I., Clement, J., Lauweryns, J. M., and Van de Woestijne, K. P. (1992). The senile lung: comparison with normal and emphysematous lungs 1. structural aspects. *Chest*, 101(3):793–799. [Cited on page 7.]
- Wahba, W. (1983). Influence of aging on lung function-clinical significance of changes from age twenty. *Anesthesia & Analgesia*, 62(8):764–776. [Cited on page 7.]
- Weibel, E. R. (1984). The pathway for oxygen: structure and function in the mammalian respiratory system. Harvard University Press. [Cited on page 17.]

- Wijesinghe, M. and Dow, L. (2005). The effect of aging on the respiratory skeletal muscles. *Principles and Practice of Geriatric Medicine*, 2:671–683. [Cited on page 5.]
- Zaugg, M. and Lucchinetti, E. (2000). Respiratory function in the elderly. *Anesthesiology Clinics of North America*, 18(1):47–58. [Cited on pages 2, 5, and 6.]